THE ASTROPHYSICAL JOURNAL, 289:494–513, 1985 February 15

SUB-MILLIJANSKY 1.4 GHz SOURCE COUNTS AND MULTICOLOR STUDIES OF WEAK RADIO GALAXY POPULATIONS

ROGIER A. WINDHORST[1,2] AND GEORGE K. MILEY
Sterrewacht Leiden
FRAZER N. OWEN
National Radio Astronomy Observatory[3]
RICHARD G. KRON[2]
Yerkes Observatory
AND
DAVID C. KOO[2]
Department of Terrestrial Magnetism, Carnegie Institution of Washington
Received 1984 May 31; accepted 1984 September 4

ABSTRACT

A deep survey has been carried out with the VLA at 21 cm to a noise level of 45 μJy. The region chosen was the Leiden-Berkeley Deep Survey (LBDS) area Lynx.2, known to be devoid of radio sources stronger than 10 mJy. A catalog of 124 sources is presented, of which 93 form a sample complete to the 5 σ level within the -10 dB radius of the primary beam.

The normalized differential source counts show a flattening below 5 mJy. The observed counts below 1 mJy are at least 10 times larger than what would be expected from ordinary spiral and Seyfert galaxies with an unevolving radio luminosity function. Nor can the sub-millijansky counts be explained by the expected giant elliptical and quasar contribution, which dominate the counts above 10 mJy.

Optical data are used to probe the nature of the sub-millijansky radio source population. Deep identifications and calibrated photometry are made on prime-focus plates obtained in four bands with the Kitt Peak 4 m Mayall telescope. In the complete sample 41 radio sources are reliably identified, with about one-fourth of the identifications being stellar objects, including two galactic stars. The data are analyzed by comparison to similar data for the 171 identifications of the Westerbork sample stronger than 1 mJy (Kron, Koo, and Windhorst [Paper III]).

In Paper III, radio sources with $S_{1.4} \gtrsim 10$ mJy were shown to consist predominantly of quasars and red giant elliptical galaxies, while only a few blue radio galaxies are seen. In contrast, for $1 < S_{1.4} < 10$ mJy a blue radio galaxy population becomes increasingly important; these often have peculiar optical morphology indicative for interacting or merging galaxies. We show that below 1 mJy the VLA sources consist of some red galaxies, but the majority are faint blue galaxies mostly fainter than $V \approx 20$. Whereas only 35% of the radio galaxies are in the blue category above 10 mJy, this fraction rises gradually to 70% below 3 mJy.

The faint blue radio galaxy population is most likely responsible for the upturn in the source counts below 5 mJy.

Subject headings: cosmology — galaxies: photometry — luminosity function — radio sources: galaxies — radio sources: identifications

I. INTRODUCTION

The Leiden-Berkeley Deep Survey (LBDS) was carried out with the Westerbork radio telescope and resulted in a complete sample of 306 radio sources with 12 MHz flux densities in excess of 0.6 mJy (5 σ) (Windhorst, van Heerde, and Katgert 1984; hereafter Paper I).[4] This survey covered nine fields, each with an area of ~ 0.6 deg^2, for which fine-grained plates in four bands were available, all taken with the Kitt Peak 4 m Mayall telescope.

On these plates, 53% of all LBDS radio sources were reliably identified in at least two passbands (Windhorst, Kron, and Koo 1984; hereafter Paper II). About 80% of the mJy radio source identifications are galaxies; the remainder are quasars and, in a few cases, galactic stars. Photoelectrically calibrated photometry has been presented for the same plates (Kron, Koo, and Windhorst 1984; hereafter Paper III), together with several dozen spectroscopic redshifts down to $V \sim 21.5$ mag. It was shown in Paper III that more than half of the millijansky radio galaxy population consists of red "standard candle" giant elliptical galaxies (referred to as *R* galaxies), which do not show strong evidence for evolution in their optical luminosity or colors out to redshifts of at least 0.6. Below ~ 10 mJy the remaining radio galaxy population consists of some normal spiral galaxies, but most are fainter blue galaxies (referred to as *B* galaxies). The latter often have peculiar optical images (compact, interacting, or merging) and have radio powers intermediate between those of spiral and Seyfert galaxies and

[1] Now at Mount Wilson and Las Campanas Observatories of the Carnegie Institution of Washington.
[2] Visiting astronomer, Kitt Peak National Observatory, which is operated by the Association of Universities for Research in Astronomy, Inc., under contract with the National Science Foundation.
[3] The National Radio Astronomy Observatory is operated by Associated Universities, Inc., under contract with the National Science Foundation.
[4] 1 mJy $= 10^{-29}$ W Hz^{-1} m^{-2}.

the break in the radio luminosity function of elliptical galaxies ($P^* \approx 10^{25}$ W Hz^{-1} for $H_0 = 50$ km s^{-1} Mpc^{-1} and $q_0 = 0$).

From the radio point of view, the LBDS field Lynx.2 (R.A. = $8^h41^m46^s$, decl. = $+44°46'50''$, $b^{II} = +38°$) is exceptional. It contains *no* sources with a peak brightness per beam greater than 6 mJy; 57 sources have flux densities between 0.6 and 6 mJy. Therefore, it is an ideal region for carrying out an even deeper wide-field survey with the VLA, because no dynamic range problems are expected.

Here we present the results of such a survey. With an effective rms noise level of ~ 45 μJy, this new survey should include all radio sources with luminosities at 1412 MHz larger than 10^{25} W Hz^{-1} to a redshift of $z \approx 2.5$. Hence, out to this redshift, the survey should miss no powerful sources above the break in the radio luminosity function.

The purpose of the paper is twofold. First, we shall investigate whether the 1.4 GHz source counts converge all the way down to ~ 200 μJy. At this flux level, radio source populations other than the luminous elliptical galaxies and quasars could start to dominate. Second, we shall investigate the nature of the sub-millijansky population with the Mayall plates by using the identification procedure described in Paper II and the photometric procedure described in Paper III. In particular, the photometry of the sub-millijansky identifications will be compared with those of the LBDS radio galaxies in the 1–100 mJy regime.

Section II presents the radio observations and describes the procedures for radio data reduction, optical identification, and photometry. Section III tabulates the data. Section IV presents the 1462 MHz source counts. We investigate whether a significant change occurs in the slope of the counts below 100 mJy by combining all other previous 1.4 GHz counts. Section V gives the identification statistics and content. Color-magnitude and color-color diagrams are used to investigate the nature of the sub-millijansky identifications. In § VI we discuss the results.

II. THE OBSERVATIONS

a) *The* 1462 MHz *VLA Observations and Data Reduction*

i) *The VLA Observations*

The observations were carried out in two blocks of 6 hr on 1981 December 23 and 30. The VLA was used in the C-array configuration (for a description, see Thompson *et al.* 1980) at an average frequency of 1461.775 MHz (wavelength 21 cm), yielding a resolution of $\sim 15''$, which is close to the expected median angular size of millijansky radio sources (Ekers and Miley 1976; see also Paper I). Hence, few sources should be missed because of resolution effects, and the positional accuracies should be sufficient for optical identification work.

In order to minimize bandwidth smearing, which would severely decrease the effective field of view for bandwidths in excess of 10 MHz, the survey was made with the VLA in line mode. Both sets of observations were made with narrow band ("line") channels, each of width 6.25 MHz, and all separated in frequency by 6.25 MHz. When mapping each of these channels individually, the expected bandwidth smearing at the -10 dB level in the primary beam (radius $0.^\circ429$) was less than 7%. With the line receiver, only one circular polarization channel (right/right) could be used, yielding a sensitivity of ~ 45 μJy in 2×6 hr.

Calibration was carried out every 20 minutes using the point sources 3C 286 and 0828+493, and the flux density scale of Baars *et al.* (1977) was adopted. Inferior data from antenna 12 were deleted, leaving a total of 26 usable antennas.

ii) *Mapping*

All six line channels obtained during the two observing days were Fourier transformed separately and subsequently combined. The maps were made with the Amdahl-7 computer at Leiden University, using the 1024^2 fast Fourier transform as implemented in the Charlottesville VLA/IBM software package. The sampling was 2.4 points per beam. In order to explore different ranges in angular size, three sets of maps were made, each having different resolutions. The first was an untapered high-resolution (HR) map with an $11.''3$ FWHM circular beam. The second set had a Gaussian taper applied to the visibility data to give medium resolution (MR) with a $14.''7$ FWHM beam. The third was a more strongly tapered set of maps made with low resolution (LR) yielding a $24.''0$ FWHM beam. Because of the different gridding of these maps at various resolutions, we could check if any sources had aliased from the first sidelobe into the main beam. Moreover, the maps of the surrounding Lynx fields (Paper I) showed us which sources could potentially give alias problems. Only in the HR map were two faint sources aliassed into the main beam. We are therefore confident that all other sources announced in the catalog are real and that the noise in the maps is not significantly increased by aliasing of faint sources.

The maps at different resolutions were made separately for all six line channels and combined subsequently. Because the data were combined *after* the Fourier transform, the bandwidth smearing is limited to that of each single 6.25 MHz line channel, i.e., at most $\sim 7\%$ at the -10 dB radius. The same procedure was adopted in creating the antenna patterns. The inner part of these combined maps was cleaned, but only down to 4 σ, because below that level an increasing number of spurious sources are found. After the clean algorithm had converged, the source components found were restored in the remaining noise map, after convolution with a "clean" beam defined from the central part of the antenna pattern. The maps of the two different observing days were cleaned and analyzed separately in order to check for systematic errors in the positions or in the flux density scale; no systematic effects were found. The two maps were then combined.

In order to obtain the lowest possible noise, we also made a "natural-weighted" map, which weighted the (U, V)-plane only in proportion to the actual sampling density. This map was 2048^2 pixels in size and produced on the VLA array processor, where it was cleaned after combination of the individual line channels and antenna patterns, as described above. But now the clean process was performed down to 1 σ, and the resulting map had a significantly lower noise level of 29 μJy and a beam with HPBW $\sim 17''$. Because in the natural-weighted map the central source density is higher and the beam broader than in the MR map, it is closer to the confusion limit. Since the natural weighting preserves the irregular baseline coverage of the VLA, the noise distribution after the Fourier transform is irregular and structured at low signal-to-noise ratio levels, irrespective of the good quality of the calibration (see Oort and Windhorst 1984). Hence, to obtain a reliable source list and source counts, a cutoff had to be applied in the natural-weighted map at the 7 σ level ($=200$ μJy). Since this level is close to the 5 σ level of the MR map (225 μJy), and the latter map suffers less from the effects mentioned above, we decided to use the MR map as the basic map for defining a complete sample.

Figure 1*a* shows a contour plot of the inner $0.^\circ9 \times 0.^\circ9$ of the cleaned MR map. The cleaned HR, MR, and LR maps had an rms noise of 48, 45, and 52 μJy per beam, respectively. These

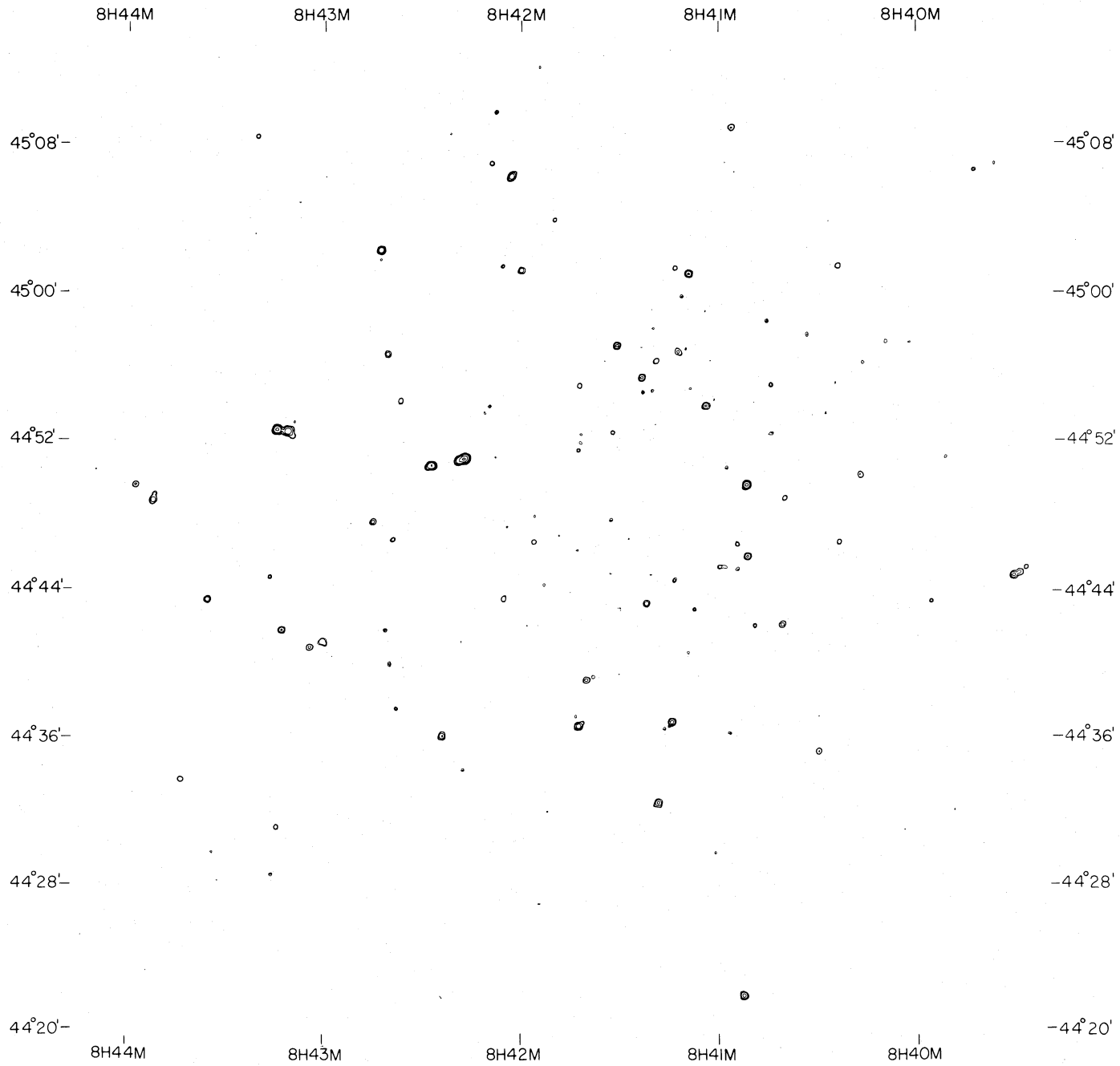

FIG. 1*a*.—Contour plots of the central 0°.9 × 0°.9 of the cleaned and restored medium-resolution (14".6) map. Contour values are $\pm 3.75\ \sigma$, $\pm 5\ \sigma$, $+10\ \sigma$, $+20\ \sigma$, $+50\ \sigma$, $+100\ \sigma$, where $\sigma = 45\ \mu$Jy per beam. Negative contours are dashed, but occur almost nowhere. The small cross in the center marks the fringe stopping center.

values did not vary by more than 4% over the individual maps. A histogram of the peak intensities in the cleaned and restored MR map is given in (logarithmic) differential and integral form in Figure 1*b*. Note the perfect Gaussian shape of the distribution of peak intensities on the negative side (parabolic shape in this representation). No negative deflections are seen below $-5\ \sigma$, and only a few between $-5\ \sigma$ and $-4\ \sigma$. This gives us confidence that the quality of the cleaned and restored maps is high enough to define a reliable sample complete at the $\gtrsim +5\ \sigma$ level. The positive tail of the distribution at the level $\gtrsim +4\ \sigma$ deviates significantly from the Gaussian noise distribution and is due to real sources. The two arrows in Figure 1*b*, at $+5\ \sigma$ and $+7\ \sigma$, mark where the sample was cut off for the source counts as described in § IV.

iii) *Source Parameters*

The source candidates were found using a point source fitting routine, which fitted the central part of the Besselian antenna pattern to all regions whose peak surface brightness on the primary beam attenuated maps, S_p, exceeded 4 times the noise. After that, source parameters were derived by least-squares fitting of the source responses using an extended ellip-

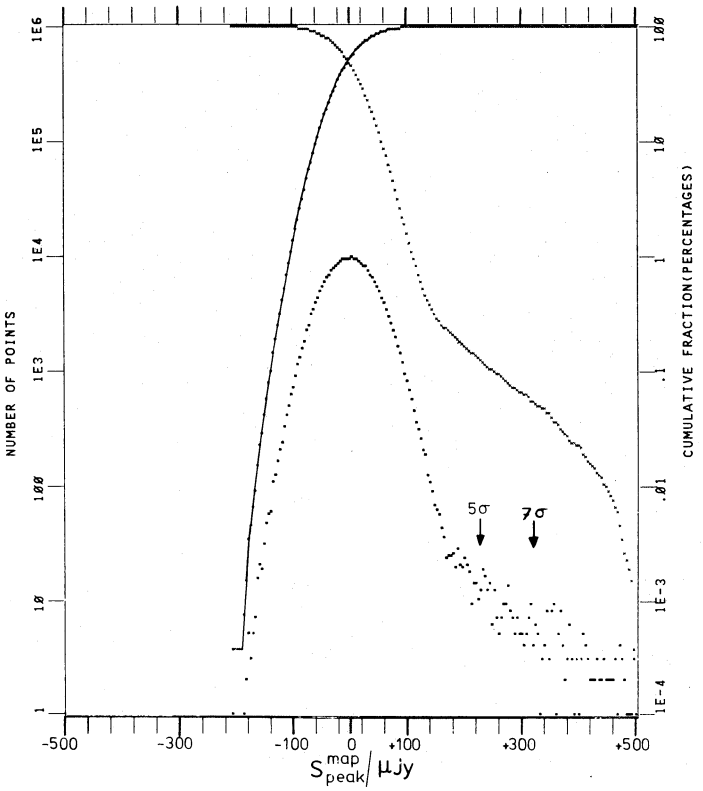

FIG. 1*b*.—Logarithmic histogram of intensities (interval of 4 μJy) in the central part (512 × 512 pixels) of the cleaned and restored medium-resolution map. Out of the 262,144 pixels, 233 have a peak flux $S_p > 0.5$ mJy and are not shown. No negative deflections are seen below $-5\ \sigma$. The lower curve is the differential distribution, the upper two are the integral distributions, starting from the positive or the negative side.

tical Gaussian. The free parameters are the position, the peak surface brightness, S_p, the Gaussian half-widths, a and b, and the position angle. The fitted Gaussian half-widths are deconvolved with the half-power widths of the beam. As discussed in detail in Paper I, the general result of noise on the least-squares Gaussian fitting algorithm is an overestimation of the source peak brightness S_p, the normalized source area or resolution parameter $R(=S_{\rm total}/S_p)$, and its angular size ψ. Although, because of noise, parameters of individual sources cannot be precisely corrected for overestimation, average statistical corrections can be made better than 5% for a large sample. In Paper I the results of a Monte Carlo test on 10240 artificial sources were used to correct the source fluxes and half-widths in a statistical sense for overestimation induced by noise. We applied the same corrections, which depend on the observed (i.e., fitted) source parameters S_p/N, R, and the major axis a. The statistical correction for the total flux can amount to 20%–30% for an individual 5 σ source.

To decide upon source resolution we used the 2 σ criterion of Paper I: a source is regarded to be resolved if its derived angular size is larger than some fraction of the beam that depends upon the signal-to-noise ratio. For resolved sources we adopted the same procedure as in Paper I to obtain an angular size ψ. To do this, the sources in the Monte Carlo simulations were conceived as unequal double sources with two pointlike components of separation ψ, position angle ϕ, and fractional flux in the strongest component f. The slight difference between the VLA beam in our MR map and the WSRT beam actually used in the Monte Carlo simulations may lead to a slight overestimation of the angular sizes derived this way from the VLA map. For a discussion see Oort and Windhorst (1984).

The final source list was made from the 1°.75 × 1°.75 MR maps. Some additional extended sources with considerably higher signal-to-noise ratio at 24″.0 resolution were retrieved from the LR map. Table 1 lists the 124 radio sources which have $S_p > 5\ \sigma$ and are believed to be real. Out of these, 93 radio sources form a complete sample within a radius 0°.429 (attenuation of 10 dB) and with $S_p > 225$ μJy (5 σ). From this complete sample, 42 sources were previously seen in the WSRT map of Paper I with $S_p \gtrsim 600$ μJy (5 σ) and within the WSRT 5 dB attenuation contour ($r = 0°.433$).

iv) *Quality of the Radio Data*

The positions of sources derived from maps generated using the two different observing days were consistent to 0″.5 in right ascension and to 0″.1 in declination. After combining these two VLA maps, the positions found for 55 sources in common with previous Westerbork maps were consistent within 0″.1 ± 0″.3 (m.e.) in α and to 0″.1 ± 0″.2 in δ. Using the independent Westerbork positions we determined the position error distribution empirically as described in Paper I. The position errors are proportional to the normalized source area, R, and inversely proportional to S_p/N, and amount to 8% of the beamwidth for a 5 σ point source. A baseline-independent calibration error of 0″.5 in the absolute positions is added in quadrature. The resulting typical position errors are of the order 1″–2″ for the faintest sources. In Figure 4 of Paper I we give a comparison of the VLA and WSRT positions. A more detailed discussion of instrumental effects at very low flux levels is given by Oort and Windhorst (1984).

The flux densities of the sources were corrected for the attenuation of the VLA primary beam using the measurements of Napier and Rots (1982). The resulting corrected 1462 MHz VLA flux densities were on average 2.5% lower than the 1412 MHz Westerbork flux densities for the 55 sources they had in common. For an average spectral index $\alpha = 0.75$ ($S \propto \nu^{-\alpha}$), the average flux scales agree to better than 1%. The errors in total flux were determined using the independently measured Westerbork fluxes. The relative error in total flux is inversely proportional to S_p/N, while a 3.5% error in the flux calibration is added in quadrature.

We reconstructed the VLA primary beam by comparing the observed VLA map fluxes $S_{\rm map}^{\rm VLA}$ with the corrected sky fluxes $S_{\rm sky}^{\rm WSRT}$ of these sources in the Westerbork map, which were transformed to 1462 MHz assuming a spectral index of 0.75. We could trace the VLA primary beam out to the first sidelobe ($r \approx 0°.85$). For sources beyond the first zero ($r \gtrsim 0.55$) an accurate Westerbork flux was retrieved from the adjacent LBDS fields (Paper I).

The resulting VLA primary beam is shown in Figure 2 as a plot of $S_{\rm map}^{\rm VLA}/S_{\rm sky}^{\rm WSRT}$ versus the radial distance r to the pointing center. The symbols denote different values of the combined signal-to-noise ratio $\Sigma = [(\mathrm{S/N})_{\rm VLA}^{-2} + (\mathrm{S/N})_{\rm WSRT}^{-2}]^{-1/2}$. The value of Σ^{-1} is proportional to the error in $S_{\rm map}^{\rm VLA}/S_{\rm sky}^{\rm WSRT}$. The points with highest values of Σ follow the measured primary beam of Napier and Rots (*full drawn line*) most accurately. Therefore, no systematic errors in the flux density scale nor in the source count weights are expected as a result of VLA primary beam uncertainties out to the 10 dB attenuation contour. A detailed comparison of the VLA and WSRT flux densities is made by Oort and Windhorst (1984).

TABLE 1

THE SOURCE LIST

NAME	RA(1950.0) H M S	DEC(1950.0) ° ' "	S1462 (MJY)	RES	PSI (")	PA (O)	CHI (")	F	SSKY (MJY)	SP/N	R	ATTEN WEIGHT	NR	NOTES
0837+44.01	8 37 26.41 0.05	44 50 37.6 0.5	182.3 46.1	R	16.0 2.1	95 7	3.1	0.60	182.3 46.1	68.70	1.77	33.37 0.00	1	*
0837+44.02	8 37 29.21 0.18	44 27 26.8 1.6	22.3 6.6	R	17.3 6.5	72 9	0.0	0.50	22.9 6.8	6.47	2.16	36.56 0.00	2	*
0837+45.01	8 37 40.13 0.12	45 1 30.4 1.1	37.7 10.2	R	17.3 5.5	94 6	8.2	0.50	37.3 10.0	10.56	2.33	33.87 0.00	3	*
0837+45.02	8 37 52.26 0.26	45 27 10.2 2.3	143.1 45.6	R	16.8 6.6	92 5	12.6	0.50	151.5 48.2	5.15	2.59	253.71 0.00	4	*
0838+44.01	8 38 37.74 0.15	44 16 37.9 1.3	22.5 6.5	R	14.5 6.5	87 6	6.5	0.50	23.3 6.7	7.32	1.99	35.56 0.00	5	*
0838+45.01	8 38 47.40 0.06	45 23 12.9 0.6	113.3 28.8	R	17.3 2.8	86 6	14.6	0.50	113.3 28.8	31.41	2.45	32.86 0.00	6	*
0838+45.02	8 38 49.16 0.26	45 36 23.0 2.2	304.0 89.2	R	18.5 6.2	90 5	22.1	0.50	343.2 100.6	6.70	3.28	348.11 0.00	7	*
0838+44.02	8 38 50.49 0.12	44 19 57.8 1.1	28.4 8.3	R	12.9 6.7	94 6	0.0	0.69	31.1 9.0	6.94	1.50	66.52 0.00	8	*
0839+44.01*	8 39 28.05 0.10	44 44 58.3 1.4	22.4 1.5	E	47.8	123	3.3	0.63	22.4 1.5	16.77	3.33	8.97 1.00	9	
A	8 39 26.28 0.09	44 45 14.0 0.8	3.05 0.53						3.05 0.53	7.21	0.98	9.63 1.26		
C	8 39 28.05 0.06	44 44 58.3 0.6	5.26 0.67						5.26 0.67	13.54	0.97	8.97 1.01		
B	8 39 30.05 0.06	44 44 47.7 0.6	14.1 1.5						14.1 1.5	27.58	1.38	8.27 1.00		
0839+45.01	8 39 42.20 0.09	45 6 40.4 0.8	9.09 1.83	U	< 9.3				9.36 1.88	6.81	0.98	31.16 0.00	10	*
0839+44.02	8 39 50.84 0.12	44 51 14.4 1.1	0.91 0.19	U	<12.8				1.00 0.21	5.06	1.06	4.15 2.74	11	
0839+44.03	8 39 55.15 0.09	44 43 26.1 0.8	1.05 0.17	U	< 9.4				1.08 0.18	6.87	0.97	3.62 1.83	12	
0840+44.01	8 40 1.19 0.36	44 57 27.6 3.2	1.80 0.52	R	18.7 6.1	103 14	2.8	0.50	1.85 0.54	3.61	2.56	4.46 0.00	13	
0840+44.02	8 40 9.00 0.10	44 57 28.7 1.0	0.91 0.17	U	<11.6				0.97 0.19	5.75	1.03	3.67 2.34	14	
0840+44.03	8 40 15.99 0.12	44 56 19.4 1.1	0.67 0.14	U	<14.3				0.79 0.16	5.19	1.16	2.92 3.27	15	
0840+44.04	8 40 16.55 0.07	44 50 16.6 0.7	1.33 0.14	U	<11.0				1.33 0.14	12.09	1.08	2.28 1.28	16	
0840+44.05	8 40 17.16 0.09	44 46 57.2 0.8	0.37 0.07	U	< 9.6				0.38 0.07	5.42	0.67	2.19 7.79	17	#
0840+44.06	8 40 22.88 0.08	44 46 38.7 0.8	0.79 0.11	U	<11.8				0.84 0.11	8.37	1.12	1.99 1.90	18	
0840+45.01	8 40 23.42 0.09	45 1 32.8 0.8	1.97 0.27	U	<12.2				2.00 0.28	9.11	1.25	3.93 1.16	19	
0840+44.07	8 40 26.61 0.40	44 58 25.3 3.6	1.05 0.26	R	22.4 11.1	83 9	7.5	0.50	1.20 0.30	4.16	1.99	2.79 0.00	20	
0840+44.08	8 40 29.28 0.07	44 35 19.2 0.7	1.57 0.18	U	<12.6				1.57 0.18	11.56	1.11	2.73 1.20	21	
0840+44.09	8 40 32.73 0.17	44 57 50.5 1.5	0.79 0.16	U	<18.1				0.91 0.19	5.12	1.63	2.44 2.75	22	
0840+44.10	8 40 39.42 0.08	44 49 1.7 0.7	0.62 0.08	U	< 8.1				0.63 0.08	8.90	1.00	1.58 2.19	23	
0840+44.11	8 40 40.22 0.06	44 42 11.2 0.6	1.24 0.11	U	< 8.5				1.24 0.11	15.25	1.09	1.66 1.33	24	
0840+45.02	8 40 40.48 0.14	45 0 27.5 1.3	0.59 0.15	U	<11.3				0.72 0.18	4.07	1.39	2.66 0.00	25	
0840+44.12*	8 40 42.07 0.28	44 52 14.4 4.2	1.02 0.21	E	56.2	34	26.7	0.80	1.02 0.21	6.01	2.30	1.64 2.94	26	
A	8 40 40.30 0.13	44 51 46.6 1.2	0.21 0.05						0.21 0.05	4.22	0.66	1.66 0.00		
B	8 40 43.26 0.13	44 52 33.1 1.2	0.81 0.13						0.81 0.13	6.73	1.64	1.63 2.63		
0840+44.13*	8 40 42.09 0.50	44 33 48.8 7.5	1.21 0.39	E	27.5	165	15.2	0.58	1.21 0.39	5.03	2.09	2.56 2.24	27	
A	8 40 41.79 0.13	44 34 1.2 1.2	0.70 0.14						0.70 0.14	5.18	1.19	2.52 3.03		
B	8 40 42.43 0.12	44 33 34.8 1.1	0.51 0.11						0.51 0.11	4.84	0.90	2.60 0.00		
0840+44.14	8 40 43.60 0.11	44 55 9.6 1.0	0.61 0.10	U	<17.7				0.69 0.11	6.65	1.27	1.82 2.76	28	
0840+44.15	8 40 44.89 0.09	44 58 35.4 0.8	0.51 0.08	U	<10.4				0.53 0.09	6.81	0.80	2.19 3.24	29	
0840+45.03	8 40 46.63 0.13	45 34 53.8 1.2	34.3 9.4	R	16.7 5.7	95 7	9.4	0.50	34.2 9.3	9.77	2.30	34.05 0.00	30	*
0840+44.16	8 40 48.55 0.08	44 42 6.7 0.8	0.44 0.06	U	< 9.3				0.45 0.07	7.29	0.92	1.50 3.45	31	

TABLE 1—*Continued*

NAME	RA(1950.0) H M S	DEC(1950.0) ° ′ ″	S1462 (MJY)	RES	PSI (″)	PA (°)	CHI (″)	F	SSKY (MJY)	SP/N	R	ATTEN WEIGHT	NR	NOTES
0840+44.17	8 40 50.71 0.05	44 45 52.4 0.5	1.65 0.10	U	< 5.9				1.65 0.10	27.04	1.00	1.36 1.11	32	
0840+44.18	8 40 50.98 0.05	44 49 44.6 0.5	4.64 0.23	U	< 4.0				4.64 0.23	74.53	1.01	1.38 1.00	33	
0840+44.19	8 40 52.13 0.05	44 22 9.5 0.5	22.5 2.7	R	7.6 3.6	135 45	6.1	0.50	22.5 2.7	29.67	1.19	14.24 0.00	34	*
0840+44.20	8 40 53.83 0.09	44 46 32.6 0.8	0.42 0.06	U	<11.4				0.46 0.07	7.40	1.07	1.30 3.73	35	
0840+44.21	8 40 53.83 0.15	44 45 11.0 1.3	0.41 0.08	U	<14.6				0.47 0.09	5.39	1.48	1.32 7.00	36	
0840+45.04	8 40 55.88 0.08	45 8 58.4 0.7	4.74 0.62	U	<13.4				4.74 0.62	11.41	1.33	6.96 1.00	37	V
0840+44.22	8 40 56.21 0.12	44 36 19.1 1.1	0.47 0.09	U	<11.5				0.53 0.10	5.47	1.19	1.83 4.42	38	
0840+44.23	8 40 57.06 0.10	44 50 40.8 0.9	0.28 0.05	U	<10.9				0.29 0.05	6.17	0.80	1.31 7.75	39	
0840+44.24*	8 40 58.37 0.25	44 45 17.4 3.7	0.93 0.17	E	20.7	85	5.1	0.58	0.93 0.17	5.58	2.98	1.25 5.68	40	
A	8 40 57.34 0.13	44 45 16.5 1.2	0.39 0.09						0.39 0.09	4.59	1.39	1.27 0.00		#
B	8 40 59.28 0.14	44 45 18.2 1.3	0.55 0.09						0.55 0.09	6.19	1.59	1.24 4.77		
0841+44.01	8 41 0.52 0.11	44 29 51.4 1.0	0.57 0.11	U	<11.5				0.59 0.12	5.39	0.81	3.04 3.94	41	
0841+44.02	8 41 0.91 0.11	44 54 20.5 1.0	0.27 0.06	U	<11.5				0.28 0.06	5.05	0.87	1.44 11.33	42	
0841+44.03	8 41 2.24 0.12	44 56 26.5 1.1	0.24 0.06	U	<12.7				0.26 0.06	4.46	0.80	1.59 0.00	43	
0841+44.04	8 41 3.39 0.05	44 54 0.4 0.6	1.91 0.12	R	7.7 3.9	93 6	1.6	0.50	1.91 0.12	25.12	1.22	1.39 1.14	44	V
0841+44.05	8 41 3.72 0.18	44 59 8.7 1.6	0.40 0.10	U	<19.9				0.49 0.12	4.14	1.39	1.88 0.00	45	
0841+44.06	8 41 6.88 0.09	44 42 59.9 0.9	0.33 0.05	U	<10.4				0.35 0.06	6.37	1.01	1.21 6.40	46	
0841+44.07	8 41 8.21 0.11	44 54 57.0 1.0	0.29 0.06	U	<10.9				0.30 0.06	5.02	0.97	1.39 11.15	47	
0841+45.01	8 41 8.61 0.05	45 1 8.8 0.6	2.71 0.20	R	6.8 4.1	90 5	4.6	0.50	2.71 0.20	24.53	1.16	2.12 1.00	48	
0841+44.08	8 41 8.73 0.13	44 40 38.3 1.2	0.26 0.06	U	<14.7				0.31 0.07	4.69	1.16	1.29 0.00	49	*V
0841+44.09	8 41 9.52 0.08	44 57 4.8 0.8	0.43 0.08	U	< 9.2				0.45 0.08	5.96	1.02	1.56 5.34	50	#
0841+44.10	8 41 10.79 0.10	44 59 54.9 0.9	0.48 0.09	U	<10.5				0.51 0.09	5.90	1.02	1.89 3.91	51	
0841+44.11	8 41 11.83 0.07	44 56 55.6 0.7	1.35 0.12	R	9.3 5.4	90 5	8.8	0.50	1.35 0.12	13.43	1.48	1.52 1.50	52	V
0841+45.02	8 41 12.75 0.08	45 1 27.2 0.7	0.74 0.10	U	< 8.6				0.76 0.10	8.55	0.94	2.11 1.91	53	
0841+44.12	8 41 12.98 0.12	44 44 34.6 1.1	0.38 0.06	U	<15.5				0.43 0.07	6.32	1.37	1.12 6.56	54	
0841+44.13*	8 41 14.60 0.07	44 36 46.2 0.9	2.73 0.17	E	33.5	133	0.0	0.86	2.73 0.17	19.14	2.10	1.52 1.23	55	
A	8 41 13.75 0.05	44 36 54.2 0.5	2.36 0.14						2.36 0.14	32.25	1.08	1.52 1.01		
B	8 41 16.03 0.11	44 36 32.0 1.0	0.37 0.07						0.37 0.07	5.31	1.02	1.53 6.55		
0841+44.14	8 41 17.78 0.05	44 32 31.1 0.6	3.15 0.23	R	9.0 3.8	135 45	7.5	0.50	3.15 0.23	26.76	1.28	2.06 1.00	56	V
0841+44.15	8 41 18.58 0.10	44 56 25.2 0.9	0.80 0.10	U	<14.5				0.82 0.10	8.70	1.49	1.41 2.29	57	
0841+44.16	8 41 19.47 0.09	44 58 11.7 0.9	0.27 0.05	U	< 9.6				0.28 0.06	5.04	0.74	1.57 13.74	58	#
0841+44.17	8 41 19.97 0.09	44 59 9.6 0.8	0.25 0.05	U	<10.1				0.27 0.05	5.41	0.62	1.68 12.47	59	#
0841+44.18*	8 41 21.01 0.12	44 54 46.6 1.7	0.75 0.13	E	31.0	100	21.8	0.54	0.75 0.13	5.73	2.32	1.26 5.21	60	
A	8 41 19.60 0.13	44 54 49.3 1.2	0.40 0.08						0.40 0.08	5.40	1.31	1.28 7.43		
B	8 41 22.48 0.10	44 54 43.8 0.9	0.35 0.06						0.35 0.06	6.15	1.01	1.25 6.32		
0841+44.19	8 41 21.41 0.06	44 43 18.6 0.6	0.92 0.06	U	< 5.7				0.92 0.06	18.83	1.00	1.09 1.50	61	
0841+44.20	8 41 22.71 0.27	44 39 52.8 2.4	0.31 0.07	U	<23.7				0.37 0.09	4.34	1.37	1.21 0.00	62	
0841+44.21	8 41 22.85 0.05	44 55 32.0 0.5	1.61 0.09	U	< 4.7				1.61 0.09	28.73	0.96	1.30 1.11	63	

TABLE 1—*Continued*

NAME	RA(1950.0) H M S	DEC(1950.0) ° ′ ″	S1462 (MJY)	RES	PSI (″)	PA (°)	CHI (″)	F	SSKY (MJY)	SP/N	R	ATTEN WEIGHT	NR	NOTES
0841+44.22	8 41 26.75 0.09	44 46 47.3 0.9	0.18 0.04	U	< 9.4				0.19 0.04	5.02	0.78	1.03 157.63	64	* #
0841+44.23	8 41 30.44 0.05	44 57 16.4 0.5	1.75 0.10	U	< 4.7				1.75 0.10	28.90	0.96	1.40 1.07	65	
0841+44.24	8 41 31.71 0.08	44 52 34.9 0.8	0.35 0.05	U	< 9.0				0.36 0.05	7.54	0.96	1.10 4.86	66	
0841+44.25	8 41 32.28 0.09	44 47 50.5 0.9	0.25 0.04	U	<10.2				0.26 0.04	6.53	0.87	1.01 11.11	67	
0841+44.26	8 41 33.02 0.11	44 45 43.3 1.0	0.19 0.05	U	< 9.1				0.20 0.05	4.18	0.99	1.01 0.00	68	
0841+44.27*	8 41 38.81 0.14	44 39 15.4 2.0	1.42 0.15	E	24.6	121	3.5	0.75	1.42 0.15	9.79	2.75	1.18 2.40	69	
A	8 41 37.66 0.11	44 39 22.8 1.0	0.36 0.07						0.36 0.07	5.01	1.28	1.18 16.27		#
B	8 41 39.64 0.07	44 39 10.2 0.7	1.06 0.09						1.06 0.09	13.69	1.46	1.19 1.76		
0841+44.28*	8 41 41.43 0.29	44 52 1.8 4.3	0.98 0.17	E	51.6	172	17.1	0.51	0.98 0.17	5.81	3.56	1.06 8.93	70	
A	8 41 41.39 0.15	44 52 28.8 1.3	0.35 0.07						0.35 0.07	5.19	1.40	1.07 20.03		
C	8 41 41.43 0.10	44 52 1.8 0.9	0.27 0.05						0.27 0.05	5.69	0.98	1.06 15.53		
B	8 41 42.09 0.10	44 51 37.6 0.9	0.37 0.06						0.37 0.06	6.63	1.18	1.05 6.80		
0841+44.29	8 41 41.76 0.08	44 55 6.7 0.7	0.48 0.06	U	<10.2				0.50 0.06	8.90	1.04	1.20 2.89	71	
0841+44.30	8 41 42.04 0.05	44 36 41.1 0.6	2.85 0.16	R	9.2 3.0	105 16	0.0	0.50	2.85 0.16	33.67	1.38	1.37 1.03	72	
0841+44.31	8 41 42.41 0.13	44 46 13.7 1.2	0.20 0.04	U	<12.6				0.23 0.05	4.67	1.11	1.00 0.00	73	
0841+44.32	8 41 42.89 0.09	44 37 11.9 0.9	0.32 0.06	U	<10.2				0.37 0.07	5.33	1.11	1.32 10.87	74	#
0841+44.33	8 41 44.76 0.09	44 45 34.0 0.8	0.18 0.03	U	< 9.2				0.19 0.04	5.60	0.72	1.00 46.04	75	* #
0841+45.03	8 41 49.51 0.08	45 4 2.6 0.7	0.63 0.09	U	< 9.8				0.65 0.09	8.38	0.72	2.40 2.28	76	
0841+44.34	8 41 50.74 0.17	44 45 41.6 1.5	0.22 0.05	U	<18.5				0.23 0.05	5.04	0.89	1.00 201.22	77	* @
0841+44.35	8 41 53.64 0.15	44 27 5.0 1.3	0.65 0.16	U	<15.6				0.80 0.19	4.36	1.19	3.41 0.00	78	
0841+45.04	8 41 54.44 0.14	45 12 9.1 1.2	2.33 0.52	U	<13.4				2.76 0.61	5.10	1.27	9.54 1.64	79	
0841+44.36	8 41 55.64 0.07	44 46 40.0 0.7	0.36 0.04	U	< 8.4				0.37 0.04	9.90	0.83	1.00 3.35	80	
0841+44.37	8 41 57.09 0.14	44 0 51.9 1.3	19.5 5.6	R	14.0 6.6	98 9	0.0	0.50	20.4 5.9	7.25	1.85	33.99 0.00	81	*
0841+44.38	8 41 57.77 0.12	44 42 8.0 1.1	0.15 0.03	U	<13.3				0.15 0.03	4.78	0.68	1.06 0.00	82	
0841+45.05	8 41 59.64 0.06	45 1 20.3 0.6	1.71 0.14	R	11.1 5.5	109 10	0.0	0.86	1.71 0.14	18.36	1.10	1.89 1.14	83	
0842+45.01	8 42 2.81 0.05	45 6 22.5 0.5	7.40 0.60	R	10.3 2.9	128 14	0.0	0.50	7.40 0.60	40.58	1.26	3.23 1.00	84	
0842+44.01	8 42 4.92 0.09	44 43 35.6 0.8	0.53 0.06	R	14.4 6.6	140 15	0.0	0.76	0.54 0.06	9.13	1.27	1.04 3.15	85	
0842+45.02	8 42 5.42 0.10	45 1 33.2 1.0	0.53 0.09	U	<12.5				0.61 0.10	6.23	1.12	1.95 3.30	86	
0842+45.03	8 42 7.50 0.09	45 9 47.0 0.8	1.57 0.27	U	< 9.7				1.64 0.29	6.80	0.92	5.87 1.58	87	
0842+44.02	8 42 7.55 0.11	44 51 14.7 1.0	0.16 0.03	U	<12.7				0.17 0.03	5.03	0.70	1.07 68.54	88	*
0842+45.04	8 42 8.75 0.12	45 7 3.4 1.1	1.48 0.25	U	<15.7				1.63 0.28	6.74	1.49	3.64 1.47	89	
0842+44.03*	8 42 10.12 0.22	44 53 50.4 3.3	0.73 0.14	E	26.7	140	0.0	0.53	0.73 0.14	5.43	2.53	1.18 7.61	90	
A	8 42 9.29 0.11	44 54 0.8 1.0	0.34 0.06						0.34 0.06	5.62	1.14	1.19 8.99		
B	8 42 10.92 0.14	44 53 40.5 1.3	0.38 0.07						0.38 0.07	5.27	1.38	1.18 10.67		
0842+44.04	8 42 17.22 0.09	44 34 19.6 0.9	0.33 0.05	U	<11.5				0.35 0.06	6.56	0.67	1.76 5.36	91	
0842+44.05	8 42 17.31 0.05	44 51 10.3 0.5	11.8 0.5	R	16.8 1.8	101 12	5.8	0.57	11.8 0.5	123.16	1.91	1.12 1.00	92	
0842+44.06	8 42 17.36 0.09	44 12 2.3 0.8	29.1 8.2	U	< 8.5				30.4 8.5	5.14	0.94	132.15 0.00	93	* #
0842+44.07	8 42 23.62 0.05	44 36 10.0 0.6	1.93 0.13	R	9.5 4.5	139 21	0.0	0.76	1.93 0.13	23.75	1.13	1.61 1.10	94	

TABLE 1—*Continued*

NAME	RA(1950.0) H M S	DEC(1950.0) ° ′ ″	S1462 (MJY)	RES	PSI (″)	PA (°)	CHI (″)	F	SSKY (MJY)	SP/N	R	ATTEN WEIGHT	NR	NOTES
0842+44.08	8 42 27.17 0.05	44 50 48.5 0.5	4.38 0.20	R	11.4 2.1	94 6	4.2	0.50	4.38 0.20	57.08	1.45	1.18 1.00	95	
0842+44.09	8 42 36.39 0.13	44 54 18.3 1.2	0.87 0.12	R	13.4 6.5	121 32	8.7	0.50	0.91 0.13	7.58	1.84	1.46 2.56	96	
0842+44.10	8 42 37.63 0.12	44 37 39.5 1.1	0.48 0.09	U	<12.7				0.55 0.10	5.93	1.26	1.65 3.99	97	
0842+44.11	8 42 38.80 0.11	44 46 48.4 1.0	0.46 0.07	U	<13.3				0.51 0.08	7.02	1.29	1.26 3.95	98	
0842+44.12	8 42 39.61 0.18	44 40 3.8 1.6	0.60 0.11	R	14.0 6.6	50 40	4.3	0.54	0.66 0.13	5.46	1.83	1.48 4.41	99	
0842+44.13	8 42 40.45 0.06	44 56 50.4 0.6	1.38 0.11	U	< 8.4				1.38 0.11	17.42	1.01	1.74 1.21	100	
0842+44.14	8 42 40.90 0.09	44 41 52.3 0.9	0.38 0.06	U	< 9.6				0.40 0.06	6.44	0.98	1.40 4.79	101	V
0842+45.05	8 42 42.47 0.11	45 1 55.3 1.0	0.56 0.12	U	<10.7				0.59 0.12	5.15	0.98	2.59 3.92	102	
0842+45.06	8 42 42.58 0.05	45 2 26.1 0.5	6.05 0.45	U	< 4.3				6.05 0.45	49.45	1.00	2.73 1.00	103	
0842+44.15	8 42 44.91 0.06	44 47 46.2 0.6	0.95 0.08	U	< 8.3				0.95 0.08	15.56	1.01	1.35 1.48	104	
0843+44.01*	8 43 2.06 0.16	44 41 5.4 2.2	3.75 0.03	E	44.8	112	10.0	0.60	3.75 0.03	10.92	4.09	1.88 1.50	105	
A	8 43 0.14 0.15	44 41 13.8 1.3	1.96 0.24						1.96 0.24	9.29	2.58	1.82 1.71		
B	8 43 4.02 0.07	44 40 56.9 0.7	1.79 0.17						1.79 0.17	13.73	1.50	1.94 1.29		
0843+44.02	8 43 8.95 0.10	44 53 13.0 0.9	0.50 0.09	U	<10.2				0.53 0.10	5.76	0.98	2.09 3.80	106	
0843+44.03*	8 43 12.67 0.19	44 52 43.9 2.4	17.7 0.2	E	35.9	84	0.0	0.60	17.7 0.2	51.72	3.51	2.18 1.00	107	
A	8 43 10.97 0.05	44 52 41.9 0.6	8.28 0.56						8.28 0.56	42.43	2.06	2.12 1.00		
B	8 43 14.33 0.05	44 52 45.8 0.5	9.48 0.63						9.48 0.63	64.82	1.46	2.24 1.00		
0843+44.04	8 43 12.68 0.05	44 41 54.2 0.5	2.31 0.17	U	< 5.1				2.31 0.17	25.81	0.93	2.14 1.00	108	
0843+44.05	8 43 14.00 0.08	44 31 12.4 0.8	1.80 0.27	U	<10.8				1.89 0.28	8.39	1.06	4.77 1.21	109	
0843+44.06	8 43 15.48 0.17	44 28 42.0 1.5	2.19 0.43	U	<22.1				2.54 0.50	5.88	1.14	7.27 1.39	110	@
0843+44.07	8 43 16.21 0.12	44 44 46.6 1.1	0.67 0.12	U	<12.1				0.75 0.13	6.15	1.29	2.13 2.68	111	
0843+45.01	8 43 20.38 0.09	45 8 35.5 0.8	5.19 0.92	U	<11.6				5.66 1.00	7.53	1.08	15.48 0.00	112	*
0843+44.08	8 43 35.39 0.06	44 43 32.5 0.6	2.85 0.26	U	< 6.4				2.85 0.26	19.86	1.02	3.15 1.00	113	
0843+44.09	8 43 43.14 0.10	44 33 47.4 0.9	4.43 0.67	R	10.0 6.5	79 12	5.7	0.50	4.57 0.70	8.73	1.49	7.85 1.01	114	
0843+44.10*	8 43 51.81 0.10	44 49 3.7 1.4	6.91 0.57	E	22.1	160	5.2	0.80	6.91 0.57	13.30	2.40	4.83 1.00	115	#
A	8 43 51.38 0.09	44 49 16.2 0.8	1.37 0.27						1.37 0.27	5.70	1.05	4.78 2.04		#
B	8 43 52.09 0.06	44 48 55.4 0.6	5.57 0.58						5.57 0.58	17.77	1.35	4.87 1.00		#
0843+44.11	8 43 57.50 0.06	44 49 45.2 0.6	3.64 0.44	U	<10.3				3.64 0.44	12.97	1.05	5.98 1.01	116	
0844+44.01	8 44 9.72 0.12	44 50 34.1 1.1	1.62 0.38	U	<12.3				1.71 0.40	4.73	0.80	10.04 0.00	117	
0844+44.02	8 44 10.41 0.12	44 15 13.4 1.1	46.8 13.2	R	14.0 6.6	116 15	0.0	0.62	48.9 13.9	7.79	1.66	84.40 0.00	118	*
0844+44.03	8 44 17.84 0.12	44 14 32.4 1.1	31.6 9.0	R	11.4 6.6	124 34	7.3	0.50	33.5 9.5	7.69	1.61	60.24 0.00	119	*
0844+44.04	8 44 21.52 0.14	44 37 15.7 1.3	7.29 1.66	U	<12.7				8.41 1.92	5.35	1.37	25.55 0.00	120	*
0844+45.01	8 44 23.68 0.15	45 21 21.5 1.3	11.9 3.8	U	<13.5				13.8 4.4	5.15	1.42	42.20 0.00	121	*
0845+44.01	8 45 16.11 0.16	44 13 4.3 1.5	11.4 3.7	U	<14.7				13.3 4.3	5.09	1.55	37.49 0.00	122	*
0845+45.01	8 45 47.31 0.05	45 1 17.2 0.5	184.5 46.7	R	14.2 2.1	93 6	6.7	0.50	184.5 46.7	61.08	1.75	38.47 0.00	123	*
0846+44.01	8 46 15.92 0.08	44 34 23.1 0.8	52.9 13.8	R	16.4 4.5	96 8	8.5	0.50	52.9 13.8	15.97	2.15	34.41 0.00	124	*

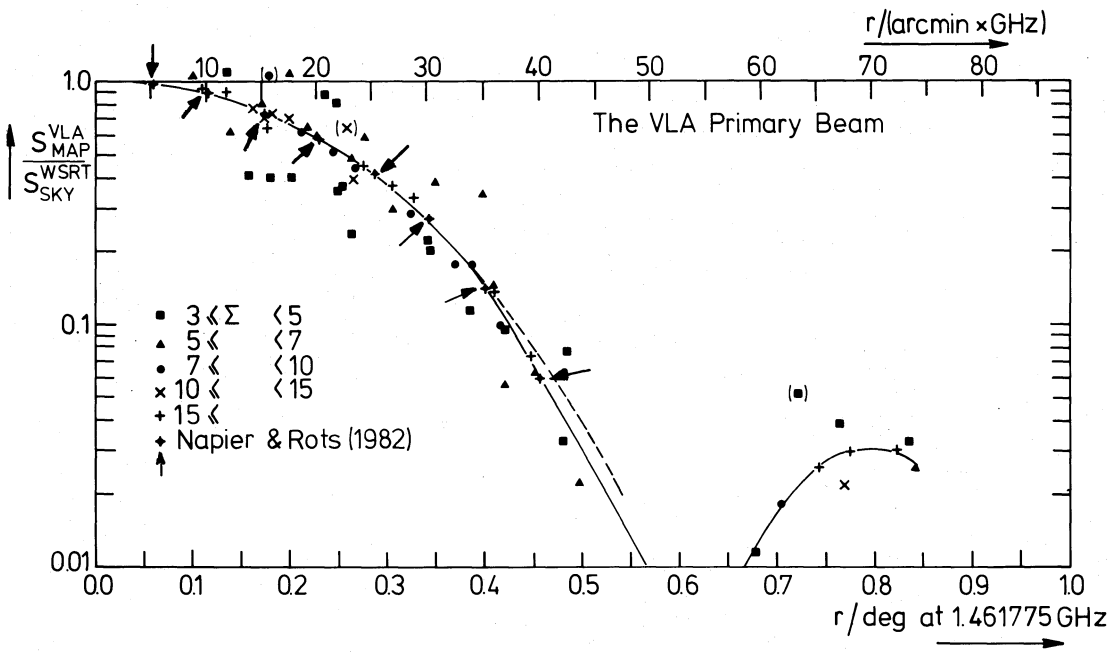

FIG. 2.—The VLA primary beam. Points are measured values of $S^{VLA}_{map}/S^{WSRT}_{sky}$, as a function of radial distance r to the pointing center and are shown for different values of the combined signal-to-noise ratio, Σ. A best fit through these data is shown by the dashed line. The solid line is the best fit through the direct measurements of Napier and Rots (1982). Beyond $r \gtrsim 0.^{\circ}6$ the first sidelobe is seen, shown here schematically by the solid line.

b) The Optical Identification Procedure

The optical identification procedure is identical to the one described on Paper II. Details can be found in that paper. Here we summarize only the information needed to judge the reliability of the current sample.

Our *UJFN* color system is based on the following emulsion and filter combinations that we used for the Mayall 4 m plates: *U*, IIIa-J + UG5; *J*, IIIa-J + GG 385; *F*, 127−02 + GG 495; *N*; IV-N + RG 695. The plates are sky limited and have the following typical exposure times and limiting magnitudes: *U*, 23.5 mag in 150 minutes; *J*, 23.7 mag in 45 minutes; *F*, 22.7 mag in 65 minutes; and *N*, 21.1 mag in 60 minutes. These limits are slightly better for stellar objects and worse for low surface brightness galaxies.

We used the Madison PDS microdensitometer for the astrometry, which was done in two stages. First, positions were measured to within 0.″4 for ∼35 secondary standard stars on Lick Astrograph plates of nearly the same epoch as the 4 m plates, using ∼30 primary standard stars from the AGK3 catalog, whose positions were corrected for proper motion to the epoch of the Astrograph plate. Second, good solutions were obtained over the 4 m plates with second-order polynomial fits, after correcting for geometrical distortion. Paper II shows that systematic astrometry errors do not exceed 0.″2–0.″3, while random astrometry errors are ∼0.″4. Allowing for minor uncertainties in the AGK3 positions, the overall astrometry error is ∼0.″5. We search for the optical object that is closest to the radio source position. In general, the likely identifications turn out not to be farther away from the radio source position than 3 times the combined radio-optical error circle.

In order to evaluate the reliability of individual identifications, as well as the reliability and completeness of the total sample, we used the likelihood ratio method of de Ruiter, Willis, and Arp (1977). Assuming that the radio source and optical candidate coincide in position, the likelihood ratio (LR) compares the probability that an optical object, once found at a certain radius from the radio source position, is the correct identification and the probability that it is a contaminating object. To calculate the likelihood ratio, the background density of objects on the 4 m plates was averaged over the values counted in PDS scans around the nonidentified radio sources; this average amounts to 13×10^{-4} objects arcsec^{-2} in the Lynx.2 field ($b^{II} = +38°$).

A complete sample of candidate identifications can be defined as (1) those optical candidates that were visible in at least two different passbands with magnitudes brighter than the plate limits, that (2) *also* have a likelihood ratio in excess of 2.0 (i.e., the probability that the candidate is the correct identification is at least 2 times the probability that it is a spurious object).

In general, the identifications of the brighter VLA radio sources that were previously detected at Westerbork turn out to be the same as the WSRT identifications in the sample of Paper II. There are two exceptions: for sources 79 and 89 in Table 1, no formal identification was found at the VLA position, although an identification was found in Paper II at the WSRT position. These sources, however, were at the edge of the field, where larger systematic errors in the VLA positions may occur (see Oort and Windhorst 1984), this resulting in a formal rejection of the candidate in the VLA sample. Two other WSRT identifications are not in our VLA list, namely 55W163 and 55W164, which are probably variable radio sources and not detected in the VLA map.

c) The Photometry

The photometry was made following the procedure described by Kron, Koo, and Windhorst (1984; Paper III) for the LBDS radio galaxies.

The first step was scanning the plate with the PDS microdensitometer at the Midwest Astronomical Data Reduction

and Analysis Facility (MADRAF) at Madison. A matrix of 80 × 80 pixels, each of 20 μm in size, was scanned in the photographic density mode on the four plates, centered on the proposed identifications. With a 4 m prime-focus scale of ∼ 18″.7 mm^{-1}, these matrices are 30″ × 30″ in size and are shown in Figure 3 (Plates 4–6), after juxtaposing the four passbands. Calibration stars and sensitometer spots were similarly scanned. The intensity after sky subtraction was then integrated in circles with radii of 5, 10, and 20 pixels around each object, from which a growth curve was constructed to check the quality of the background determination. The standard aperture for all objects was a radius of 10 pixels (7″.5 diameter). A radius of 20 pixels was used for very bright objects, and a radius of five pixels was used for some very faint objects.

A relative intensity calibration was made by transforming the measured densities into relative intensities via measurement of the sensitometer spots. Absolute calibration of the *J* plates was determined using a photoelectric sequence of SA 28 in the *B* band, kindly provided by Dr. A. Sandage. The zero points for the other bands were derived from the color distribution of common stars. In Paper III the error in tying the zero point in photographic *J* to the photoelectric sequence in *B* was estimated to be ∼0.15 mag, because the standard stars are few and relatively bright. The accuracy of the color zero points for the other passbands is probably better than 0.15 mag.

No corrections for galactic absorption have been made to the magnitudes, since the bootstrapping of color zero points from the color distribution of the stars already takes out most of the reddening. The Lynx.2 field is expected to have an absorption smaller than the error in our photometric zero point, where the former is based upon neutral hydrogen measurements.

For all identifications, the type (galaxy or stellar, irrespective of color), morphology (compact, fuzzy, elliptical, or spiral), and environment (cluster, group, or double) were noted by eye from the PDS screen and are listed in Table 2. The reliability of this classification is lower for fainter objects; virtually no classification was possible for objects within 1 mag of the plate limit. A classification index related to the apparent degree of central concentration of light (effectively the bulge-to-disk ratio for the brighter galaxies) was also made for all but the faintest galaxies (see Paper III).

III. THE DATA

a) *The Source List*

Details on the source parameter specifications are given in Paper I. The radio data are given in Table 1, which is organized as follows:

Column (*1*): The source in right ascension/declination type format. For double or multiple sources the outermost components are labeled "A" and "B," while any central component is always labeled "C." For such sources, the first line (marked with an asterisk) gives the flux-weighted positions, total fluxes, and overall angular sizes.

Columns (*2*) *and* (*3*): Right ascension and declination for equinox 1950.0 and associated error.

Column (*4*): Total 1462 MHz flux density and its error, both in millijanskys and corrected for primary beam attenuation. This flux has also been corrected for overestimation induced by noise.

Column (*5*): Resolution code: U is unresolved source, R is resolved source, E is extended (double, multiple) source.

Column (*6*): For resolved and extended sources, the largest angular size, ψ, and its error, in seconds of arc, is given. For unresolved sources, only a 1 σ upper limit is given.

Column (*7*): The source position angle and its error, measured in degrees (north toward east).

Column (*8*): The deconvolved Gaussian minor axis in seconds of arc.

Column (*9*): The component flux ratio, *f*, defined as the fractional flux in the brightest component in the unequal double-source model.

Column (*10*): Total 1462 MHz flux density and its error, corrected for primary beam attenuation, but not for noise overestimation.

Column (*11*): The peak signal-to-noise ratio in the map, S_p/N, with the noise from the map where the source was found and parameters were derived.

Column (*12*): The number of uncorrelated beam areas, *R*, covered by the source.

Column (*13*): The upper number is the primary beam attenuation factor (by definition, ATT ≥ 1) using the measured relation by Napier and Rots (1982). The lower number is the corresponding weight that the source should have in the source counts and other flux density–dependent studies.

Column (*14*): Sequence number. This number refers to the photographs (Fig. 3).

Column (*15*): Notes: asterisk (*) denotes a source not in the complete sample (attenuation greater than 10.0 or $S_p/N < 5.0$); *V* is possibly variable (see also Oort and Windhorst 1984); e denotes source parameters derived from LR map; and number (※) denotes parameters derived from HR map.

b) *The Optical Data*

Details on the parameters relevant to the identification can be found in Paper II, and those relevant to the photometry in Paper III. The optical data are given in Table 2, which is organized as follows:

Column (*1*): Sequence number of the identification. An asterisk denotes a double radio source (see Table 1).

Columns (*2*) *and* (*3*): Right ascension and declination for equinox 1950.

Column (*4*): The difference $\alpha_r - \alpha_0$ (in seconds of arc) after correction for average offset $\langle \alpha_r - \alpha_0 \rangle = +0''.5$.

Column (*5*): The difference $\delta_r - \delta_0$ (in seconds of arc) after correction for average offset $\langle \delta_r - \delta_0 \rangle = -0''.2$.

Column (*6*): Position difference, normalized to the combined radio-optical error.

Column (*7*): Likelihood ratio.

Column (*8*): Object class: G denotes extended image; Q, stellar image, a question mark (?), unknown type; S, galactic star, confirmed by spectroscopy.

Column (*9*): Morphology: EL is elliptical, SP is spiral, CM is compact, FZ is fuzzy. The numbers give the estimate bulge-to-disk ratio index (Paper III).

Column (*10*): Environment: CL is a cluster, GR is a group, DB is a double galaxy.

Columns (*11*)–(*14*): Apparent magnitudes in the passbands *U*, *J*, *F*, and *N*.

Column (*15*): Notes the photometry: 4″ is the aperture used sometimes for faint objects; 15″ is the aperture for bright objects; "BOTH" indicates that two objects were unavoidably in the aperture; "EDGE" is at plate edge or close to guide probe; "EST" denotes that photometry was an eye estimate;

TABLE 2

THE OPTICAL DATA

NR	RA(1950) H M S	DEC(1950) ° ' "	DRA (")	DDEC (")	R	LR	ID	TYPE	ENVIR	U	J	F	N	NOTES (PHOT)	CODE
* 9	8 39 28.31	44 44 58.4	-2.2	0.1	1.84	14.12	Q			18.05	18.76	18.27	17.56		0
11	8 39 50.63	44 51 13.3	2.7	1.3	2.38	4.83	?			22.90		22.24	20.54		0
12	8 39 55.17	44 43 27.6	0.3	-1.3	1.36	54.82	G	SP 3		18.30	18.23	17.13	16.23	15"	0
13	8 40 1.64	44 57 28.5	-4.3	-0.7	1.10	6.07	G	SP 3		19.32	18.32	17.04	16.12	15"	2
14	8 40 8.98	44 57 28.2	0.7	0.7	0.89	63.09	G?		CL	22.47	23.21	21.58			0
16	8 40 16.81	44 50 15.9	-2.2	0.9	2.81	4.49	G	3				21.81	20.61		0
18	8 40 22.92	44 46 40.4	0.1	-1.5	1.55	41.92	Q				22.57	21.12	20.23		0
20	8 40 27.27	44 58 26.6	-6.5	-1.1	1.53	3.00	Q?			22.90		22.23	20.37	N	2
22	8 40 32.75	44 57 53.2	0.2	-2.5	1.56	13.80	G	CM 1	GR	23.00	22.49	20.21	18.95	U	0
23	8 40 39.49	44 49 2.4	-0.3	-0.5	0.65	142.33	G?				24.22	21.93	20.28		0
24	8 40 40.25	44 42 11.5	0.2	-0.1	0.24	199.52	Q			22.30	22.66	22.99			0
25	8 40 40.33	45 0 27.7	2.1	0.0	1.34	22.99	G?			22.89	23.00	22.19	20.93		2
28	8 40 43.84	44 55 10.1	-2.1	-0.3	1.62	23.02	G?				23.68	21.69	19.57		0
29	8 40 45.01	44 58 37.7	-0.8	-2.1	2.32	9.08	Q			22.05	23.10	22.47			0
33	8 40 50.99	44 49 45.0	0.4	-0.2	0.59	225.41	Q			21.74	21.21	21.17	21.33		0
34	8 40 52.12	44 22 8.9	0.6	0.8	1.45	79.67	Q?			22.66	23.21	22.44	21.01		2
36	8 40 54.24	44 45 13.0	-3.8	-1.8	2.60	2.04	?			23.54				U	1
39	8 40 57.15	44 50 38.2	-0.5	2.8	2.79	2.31	S			16.20	16.10	15.68	14.29	N	0
43	8 41 2.33	44 56 24.7	-0.4	2.0	1.72	18.58	G	SP 4		20.74	20.35	19.46	18.47		2
44	8 41 3.36	44 54 1.7	0.9	-1.1	1.78	45.06	S			15.89	16.02	15.64	13.82		0
45	8 41 3.53	44 59 8.9	2.6	0.0	1.31	17.52	G?	1		19.64	19.58	18.65	17.74		2
49	8 41 8.69	44 40 37.9	0.9	0.6	0.77	51.82	G	1		22.88	22.11	20.03	18.73		2
51	8 41 11.00	44 59 53.4	-1.8	1.7	2.23	8.44	G?			22.53	22.92	21.53			0
52	8 41 11.81	44 56 55.4	0.8	0.4	0.96	96.32	?						21.53		1
56	8 41 17.73	44 32 31.2	1.1	0.1	1.38	85.38	G	SP 4		17.15	17.11	16.25	15.45	15"	0
57	8 41 18.47	44 56 27.2	1.7	-1.8	2.21	9.61	G	EL 2		18.24	18.14	17.14	16.34	15"	0
58	8 41 19.60	44 58 9.5	-0.9	2.4	2.34	5.53	?				23.66	21.73	20.30		0
62	8 41 22.77	44 39 53.4	-0.1	-0.4	0.15	17.72	G?			22.36	23.12	22.19	20.85		2
63	8 41 22.84	44 55 32.2	0.6	0.0	0.83	171.61	G	SP 3	DB	18.82	18.70	17.80	17.00	EST	0
64	8 41 26.74	44 46 48.0	0.6	-0.5	0.69	81.93	?			23.78	22.96	22.36	22.03		0
66	8 41 31.84	44 52 35.0	-0.8	0.1	0.82	93.23	Q			22.45	22.47	22.17			0
68	8 41 33.07	44 45 45.2	0.0	-1.7	1.48	33.25	Q			18.37	18.41	18.40	17.84		2
* 70	8 41 41.37	44 52 1.4	1.2	0.6	0.40	8.58	G?			23.50	22.79	21.30	17.41		0
73	8 41 42.43	44 46 14.6	0.4	-0.7	0.56	59.30	G	EL 2		17.22	16.26	15.31	13.42		2
74	8 41 42.95	44 37 11.9	-0.2	0.2	0.29	111.41	G	3		22.21	22.15	20.88	19.55		0
75	8 41 44.73	44 45 33.6	0.8	0.6	1.05	79.39	G	FZ 4	DB	23.88	23.14	21.21	20.62		0
76	8 41 49.64	45 4 4.0	-0.9	-1.2	1.63	43.87	G	FZ 4			22.99	21.46	19.75		0
78	8 41 53.75	44 27 4.8	-0.6	0.4	0.50	45.72	?			22.91	22.70				2
80	8 41 55.72	44 46 39.9	-0.4	0.3	0.56	141.05	G	3	DB	21.74	21.31	19.86	18.69	BOTH	0
82	8 41 57.71	44 42 9.8	1.1	-1.6	1.56	25.39	G	SP 4		17.22	16.22	15.19	13.20	15"	2
84	8 42 2.86	45 6 22.6	-0.0	0.1	0.20	262.08	G	EL 1	GR	18.86	17.96	16.52	15.66	15"	0
86	8 42 5.38	45 1 34.1	1.0	-0.7	1.02	59.03	G	1	CL	22.49	22.11	20.73	19.42	BOTH	0
92	8 42 17.48	44 51 9.4	-1.2	1.1	2.34	17.37	G	CM 1	CL	22.17	21.21	19.61	18.42		0
96	8 42 36.46	44 54 20.4	-0.2	-1.9	1.30	25.67	?			23.07	24.38			UJ	1
97	8 42 37.61	44 37 37.1	0.7	2.6	2.24	6.68	G	1	GR		22.96	20.97	19.40		0
98	8 42 38.59	44 46 49.8	2.8	-1.2	2.51	4.18	Q?			22.41	23.32	22.59	21.38		0
99	8 42 39.70	44 40 8.0	-0.5	-4.0	2.37	2.56	G?			22.06	22.34	20.90	19.79		0
100	8 42 40.57	44 56 50.8	-0.7	-0.2	0.93	142.17	Q			22.61	22.94	22.11	21.14	4"	0
101	8 42 41.19	44 41 52.6	-2.6	-0.1	2.28	8.13	G	3		20.80	21.50	20.35	19.60	EST	0
102	8 42 42.78	45 1 53.7	-2.9	1.8	2.70	2.40	G	1	GR	21.66	20.61	18.86	17.76		0
104	8 42 44.87	44 47 45.8	0.9	0.6	1.44	72.05	?			22.95		22.08	20.71		0
A105	8 42 59.55	44 41 3.5	-0.4	12.0	9.21	0.0	Q			21.53	21.76	21.36	21.42		2
B105	8 43 4.03	44 40 57.0	0.6	2.7	0.46	4.31	G	CM 1		22.85	21.86	20.05	18.73		2
*107	8 43 12.65	44 52 46.2	0.2	4.8	1.94	3.93	Q?			22.82	23.55	22.14	21.24		0
A107	8 43 11.06	44 52 40.5	-2.0	-0.6	2.23	9.87	?	3		23.62	23.57	22.40	21.44	4"	2
B107	8 43 14.59	44 52 53.1	-2.1	-6.7	9.06	0.0	?			23.01	23.57				2
108	8 43 12.72	44 41 54.0	0.1	0.4	0.63	208.92	G	3		23.33		21.96	20.11		0
111	8 43 16.43	44 44 46.0	-1.8	0.8	1.51	26.94	G	SP 3		19.20	18.82	17.69	16.54	15"	0
114	8 43 43.30	44 33 46.7	-1.3	0.9	1.40	38.08	G?			22.19	21.75	20.77	19.48		0
116	8 43 57.36	44 49 45.9	2.0	-0.5	2.40	11.40	Q			20.67	21.23	20.35	19.72		0
117	8 44 9.79	44 50 34.0	-0.3	0.3	0.36	74.59	Q			20.96	19.33	17.78	16.13	EDGE	2
120	8 44 21.62	44 37 15.4	-0.6	0.5	0.53	66.11	Q			18.41		18.24	18.38	EDGE	2

U, *J*, *F*, and/or *N* means that these passbands are unreliable because the object was too faint for good photometry.

Column (*16*): The code is as follows: 0, reliable identification in complete radio-optical sample; 1, reliable identification, but not in optically complete sample; 2, reliable identification, but not in radio complete sample.

IV. THE 1.4 GHz SOURCE COUNTS

a) Method and Results

The complete sample of VLA sources with $S_p > 225$ μJy (5 σ) and within the 10 dB attenuation contour of the primary beam was used in constructing the 21 cm source counts. Complex sources or sources with multiple components were treated as one radio source if the component peak separations were smaller than two beams in the LR maps (i.e., less than 50″) and also if the optical identification or low surface brightness emission between the components suggested that the complex is actually one single source. The resulting source counts were, however, insensitive to this definition.

Every radio source was given a weight inversely proportional to the area over which it could have been seen until it dropped below the completeness limit due to primary beam attenuation (Katgert *et al.* 1973). The uncertainty in this weight is determined mainly by random errors in the source peak flux density and to a much lesser extent by uncertainties in the VLA primary beam attenuation induced by the pointing errors of the individual telescopes.

A remaining uncertainty is the correction for resolution bias (for missing low surface brightness sources) and for population bias (for the influence of noise and very faint unresolved sources on the flux-determining algorithm). A thorough discussion of these biases in confusion-limited surveys has been given by Murdoch, Crawford, and Jauncey (1973) and for noise-limited surveys by Oosterbaan (1978) and in Paper I. In our noise-limited survey the population bias manifests itself to first order as a systematic noise-induced overestimation of peak and integrated flux densities. In addition, for a δ-function–shaped input distribution of peak and integrated fluxes, the output distribution resulting from the instrument plus the algorithm is not Gaussian, but has tails toward higher flux densities. Thus, we also have to correct in a statistical sense for the fact that *more* sources with an intrinsic total flux of 4 σ are found beyond the 5 σ peak flux threshold than that sources intrinsically brighter than 5 σ are dropping below the 5 σ peak flux density cutoff.

In Paper I corrections for population and resolution bias were derived from the angular size distribution in the 1–10 mJy range in combination with a flux density contingency table. This table describes statistically the migration of sources close to the 5 σ peak flux density cutoff, caused by the asymmetrical influence of noise on the algorithm. To the VLA source weights, we applied the same corrections. In Paper I these corrections were calculated for the *same* flux determining algorithm and for the 12″.5 × 17″.6 WSRT beam, which is similar to our 14″.6 × 14″.7 VLA beam. The resulting errors in the source count weights are estimated to be ∼10% for the strongest sources, but can be larger for fainter sources. However, for bins with a large number of sources the average weight is statistically accurate.

The 5 σ source counts are presented in differential form in Table 3A, normalized to a Euclidean differential count of 225 $S^{-5/2}$ s^{-1} Jy^{-1} (Willis *et al.* 1977). The relative uncertainties in the differential counts are proportional to the sampling error in the average weight per bin: $1/n \times [\Sigma(\text{weight})^2]^{1/2}$, where n is the number of sources in that bin. The normalized differential counts are plotted in Figure 4*a*, together with data from the previous 21 cm (Westerbork and Greenbank) surveys (for references see Paper I) and the VLA points of Condon and Mitchell (1982). All 1.4 GHz counts were plotted after transformation to 1412 MHz. Points without error bars are not independent from other points plotted, and points between brackets are possibly incomplete (mostly the statistically poor, bright end of a survey). In a few surveys some of their adjacent bins are combined if the survey had fewer than 20 to 30 sources per bin. Because our particular field was choosen to be devoid of strong sources, the brightest bin in Tables 3A and 3B is systematically low and not plotted in Figure 4*a*.

The best independent check upon systematic errors is to cut the sample off at a higher S/N level, where the systematic effects are smaller. Given the uncertainties in the flux-determining algorithm and in the weights, a sample cut-off at $S_p/N = 7.0$ should be safe for the source counts. The 7 σ counts from the MR map and from the natural weighted map are given in Table 3B and in Figure 4*a* and are within the statistical errors consistent with the 5 σ counts, illustrating that the quality of the correction for population and resolution bias is largely independent of beam size and signal-to-noise ratio.

Our VLA 5 σ and 7 σ counts also agree with the deep WSRT counts from the Lynx.2 map of Oort and Windhorst (1984), which has a map noise of 60 μJy. Since both our VLA counts and their WSRT counts were derived from the *same* sources in the Lynx.2 field, any difference between the two counts *must* be of instrumental origin or due to differences in the data-reduction techniques (granting that variability can be ignored). Figure 4*a* shows that our 5 σ VLA counts are slightly (at most 20%) but not significantly higher than the 5 σ WSRT counts. The resolution correction to our 5 σ VLA counts could be slightly overestimated if the angular size distribution depends strongly on flux density around 1 mJy, in the sense that the fraction of large sources ($\psi \gtrsim 2 \times$ HPBW) is smaller below 1 mJy when compared to higher flux densities. There is some evidence for such an effect (Oort and Windhorst 1984). Since the angular size distribution in Paper I was found to be only marginally dependent on flux density in the range 1–100 mJy, the resolution correction that we applied to our VLA counts is probably not overestimated by more than 10%–20%. This is supported in Figure 4*a* by the consistency of the deep VLA and WSRT counts in the *same* Lynx.2 field done at *different* signal-to-noise ratio levels.

Figure 4*a* demonstrates the good correspondence, in general,

NOTES TO TABLE 2.—For the following VLA objects, spectroscopic redshifts have been measured thus far, following the procedure as described in Paper III. For the spiral galaxies with sequence numbers 12, 82, and 11 the redshifts are 0.12, 0.05, and 0.125, respectively. For the faint blue galaxy with number 80 the redshift is 0.425. For the elliptical galaxy numbers 57 and 102, the redshifts are 0.147 and 0.32, respectively. The latter follow the Hubble relation of giant elliptical radio galaxies (Paper III, Fig. 5) within 0.3 mag. The stellar identifications of radio sources 39 and 44 have spectra like intermediate-type stars. Redshifts of objects already seen in the Westerbork sample are given and discussed in Paper III.

TABLE 3

1462 MHz COUNTS FROM MR MAP

S (mJy)	$\langle S \rangle$ (mJy)	NH NL	$\langle WT \rangle$ + − ME	$n(S)$ (sr^{-1})	dN/dS (sr^{-1} Jy^{-1})	N/N0	$n(>S)$ (sr^{-1})
A. The 5 σ Counts							
0.275							1.37×10^6
							0.19
	0.389	23	5.26	6.98×10^5	2.54×10^9	0.033	
		0	1.20	1.59	0.58	0.007	
0.550							6.73×10^5
							0.97
	0.778	23	2.93	3.89×10^5	7.08×10^8	0.052	
		0	0.65	0.87	1.57	0.012	
1.10							2.84×10^5
							0.44
	1.56	17	1.37	1.42×10^5	1.29×10^8	0.053	
		1	0.33	0.35	0.32	0.013	
2.20							1.42×10^5
							0.28
	4.39	16	1.09	1.00×10^5	1.52×10^7	0.079	
		0	0.28	0.26	0.39	0.020	
8.80							4.17×10^4
							1.07
	17.4	3	1.00	1.73×10^4	6.55×10^5	0.109	
		0	0.58	1.00	3.78	0.063	
35.2							2.44×10^4
							0.38
B. The 7 σ Counts							
0.332							8.46×10^5
							1.84
	0.559	14	6.94	5.60×10^5	9.23×10^8	0.029	
		0	2.20	1.78	2.93	0.009	
0.939							2.86×10^5
							0.49
	1.33	12	1.75	1.21×10^5	1.30×10^8	0.036	
		0	0.54	0.38	0.40	0.011	
1.88							1.64×10^5
							0.31
	2.65	11	1.28	8.14×10^4	4.34×10^7	0.068	
		0	0.39	2.50	1.34	0.021	
3.75							8.31×10^4
							1.89
	6.30	7	1.02	4.14×10^4	6.02×10^6	0.080	
		0	0.39	1.56	2.28	0.30	
10.6							4.17×10^4
							1.07
	17.8	3	1.00	1.73×10^4	8.93×10^5	0.160	
		0	0.58	1.00	5.15	0.092	
30.0							2.44×10^4
							0.38

Col. (1).—Flux density bins.
Col. (2).—Average flux density (see Paper I).
Col. (3).—Number of sources (NH). "NL" is the number of additional sources seen only in the LR map.
Col. (4).—The average weight in this bin and its error.
Cols. (5), (6).—The differential source density.
Col. (7).—The differential counts, normalized to a Euclidean count of 225 $S^{-5/2}$ (sr^{-1} Jy^{-1}).
Col. (8).—The integral count (sr^{-1}). Normalization is from Paper I.

between the counts from the various surveys at different S/N levels. The points of Condon and Mitchell (1982) are consistent with our counts, apart from their faintest one, which is a factor 2.3 lower than our faintest points, a 2 σ difference. A deeper map of the same area suggests that this apparently lower point is possibly a statistical fluctuation (Condon 1984, private communication).

We conclude that after correcting the surface densities in a statistical sense for population and resolution bias, the resulting source counts are apparently free of major systematic effects. Figure 4*a* shows that the counts from various surveys at different S/N levels do not converge as strongly below 10 mJy as would have been expected from the counts in the 10–100 mJy regime. This apparent gradual change in slope has a second derivative value of zero occurring around 5 mJy.

b) Analysis of the 1.4 GHz *Counts*

We now examine more quantitatively whether a change in slope in the source counts is present in the data below 10 mJy. Figure 4*b* shows the same counts as Figure 4*a*, except that the

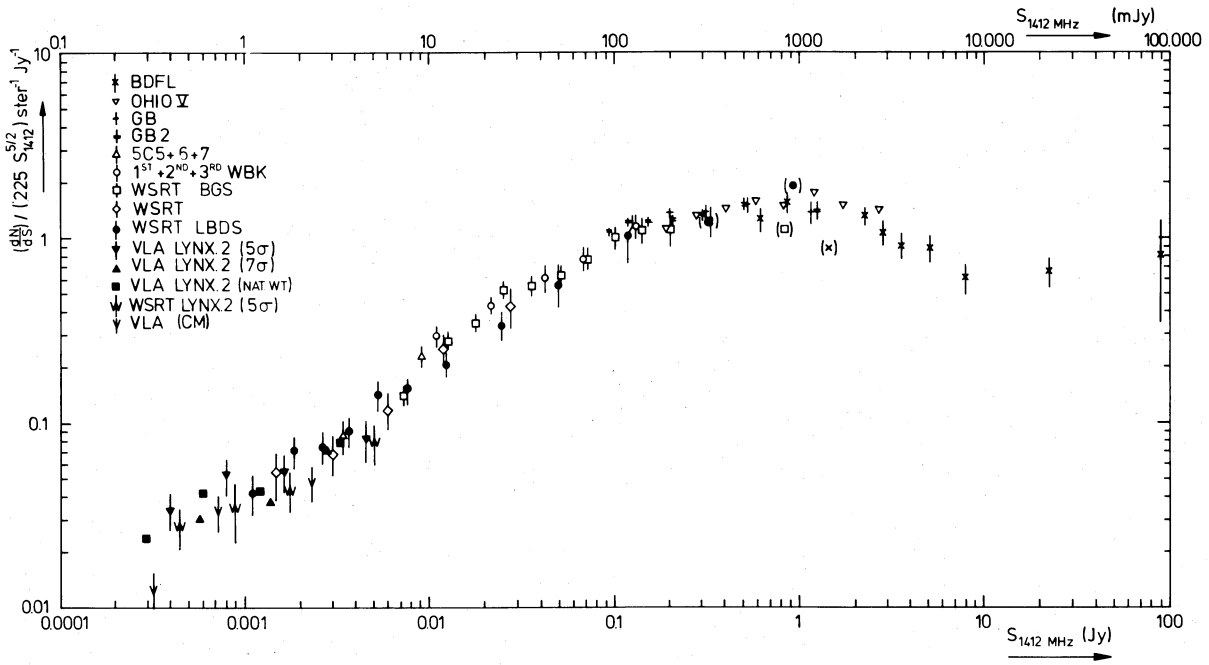

FIG. 4*a*.—The normalized differential 21 cm source counts. Open symbols are data from other 1.4 GHz surveys summarized in Paper I. All data are transformed to 1412 MHz. Filled circles are the 5 σ counts from the Leiden Berkeley Deep Survey (Paper I). Filled triangles denote the 5 σ and 7 σ counts of the current VLA survey of Lynx.2, and filled squares are the 7 σ counts from its natural weighted map. Symbols "W" denote the deep WSRT count of the Lynx.2 field of Oort and Windhorst (1984). Symbols "V" denote the VLA survey of Condon and Mitchell (1982). Error bars are only given for independent points. Points between brackets are believed to be incomplete. Fig. 4*b* on page 512.

nonindependent points are omitted, as well as a few points that may suffer from incompleteness (the brightest GA, BGS, and LBDS points at the 1 Jy level). The normalized differential counts reach their maximum for $S_{1.4} \approx 700$ mJy and have a zero second derivative around 5 mJy. For $5 < S_{1.4} < 100$ mJy the logarithmic slope of the normalized differential counts is 0.71 ± 0.03, or, if we define $dN/dS \propto S^{-\gamma}\ \mathrm{sr}^{-1}\ \mathrm{Jy}^{-1}$, then $\gamma \approx 1.8$. For $0.25 \lesssim S_{1.4} < 5$ mJy the slope is 0.41 ± 0.07, or $\gamma \approx 2.1$. The change in slope that occurs around 5 mJy is thus 0.30 ± 0.08.

Summarizing, the normalized differential 21 cm source counts in Figure 4*a* show evidence for flattening below ~ 5 mJy. This flattening corresponds to an *excess* of faint radio sources with respect to the converging part of the source counts brighter than 5 mJy. This convergence starts below ~ 1 Jy after the initial steep rise of the source counts at ~ 10 Jy and is normally interpreted as due to the shape of the epoch-dependent radio liminosity function of elliptical radio galaxies and quasars (for a review, see, e.g., van der Laan and Windhorst 1982 and van der Laan *et al.* 1983). This convergence is illustrated in Figure 4*b* by the lines indicating the contribution to the counts of these populations, as computed by Windhorst (1984) from the LBDS and other surveys. (These computations are not very sensitive to the particular choice of the world model.)

The predicted counts between 0.1 and 1000 mJy for the local nonevolving population of spiral and Seyfert galaxies, whose radio luminosity function (RLF) is summarized by Meurs (1982), are shown in Figure 4*b* by the dotted-dashed line. These counts have a nearly Euclidean slope, but lie always more than a decade below the observed counts. It is clear that local nonevolving spiral and Seyfert radio galaxies *alone cannot* explain the observed flattening of the 21 cm source counts below 5 mJy.

The quasar contribution to the 1.4 GHz counts is taken from Windhorst (1984), who reviewed the observed 1.4 GHz quasar counts for $B \lesssim 24$ and assumed that beyond $B = 24$ no significant contribution is made by quasars. The quasar contribution (*full-drawn line*) is of the order 10%–30% and is largest around the maximum in the counts at the 1 Jy level. The contribution of the evolving radio luminosity function of relatively powerful elliptical galaxies ($\log P_{1.4} \gtrsim \log P^*_{1.4} = 25$; *dotted line*) was computed from the bivariate (radio-optical) flux density distributions of the LBDS and of brighter source samples. Beyond the limits of the 4 m plates, a model extrapolation was used in these computations. The contribution expected from the giant elliptical galaxies can account for essentially all of the remaining sources in the flux density range 10 mJy $< S_{1.4} <$ 10 Jy.

The sum of the contribution to the 21 cm counts by giant elliptical galaxies, quasars, Seyfert galaxies, and normal spirals is shown by the long dashes in Figure 4*b*. The total counts are dominated by the giant elliptical radio galaxies and quasars, which can explain all of the counts for $S_{1.4} > 10$–20 mJy, but start to fail for $S_{1.4} < 5$ mJy. Their contribution below 10 mJy cannot be enhanced unless population evolution is assumed below the well-known break in the E+S0 radio luminosity function (Auriemma *et al.* 1977).

One possible interpretation of the upturn in the counts is that a new population of radio sources appears below 5 mJy. This conclusion, however, cannot be derived from the source counts *alone*. To illustrate this point, we express the counts for a particular population as

$$N(>S) = \int_0^\infty \rho(P_{1.4}, z)\, \frac{dV(z)}{dz}\, dz\ ,$$

$$\text{with } S_{1.4} = f(P_{1.4}, \alpha, z, q_0)\ ,$$

where the dependence of spectral index on redshift may com-

plicate the picture, although the effect is presumably small (Katgert-Merkelijn, Lari, and Padrielli 1980). The integrand consists of the differential volume element $dV(z)/dz$, which depends on q_0, and $\rho(P_{1.4}, z)$, the epoch-dependent radio luminosity function, the *functional form* of which may also depend on redshift. Given sufficient freedom of the integrand, *any* observed form of the counts can be reproduced by a *single* population. Therefore, to investigate the nature of the change in slope (i.e., the need for another population) one should further constrain the integrand. Precise constraints can logically come only from surveys with complete redshift coverage, which are not yet available. Only for the 3CR is the redshift information approaching completeness, but for those sources the radio-optical flux ratio is over four decades larger than for our VLA sources.

We shall approach the nature of the sub-millijansky population by studying their identifications and their multicolor photometry.

V. CONSTRAINTS FROM OPTICAL IDENTIFICATIONS AND PHOTOMETRY

a) Identification Statistics

The complete VLA sample in Lynx.2 consists of 98 radio sources ($S_p/N > 5.0$ and attenuation less than 10.0), of which five were not on the exposed part of the 4 m plates. Among the remaining 93 radio sources, 41 proposed identifications have likelihood ratios LR > 2.0. Among these, four spurious objects are expected. Only one real identification is expected to have LR < 2.0. Hence, the total identification fraction is 38/93 (41%), while the sample reliability is 90% (37 out of 41 announced identifications are correct), and its completeness is 97% (37 out of 38 expected identifications are indeed announced).

Among the 41 proposed identifications, there are two galactic stars, 10 quasars, and 29 radio galaxies or faint objects of unknown type. These proportions are not significantly different from the identification content of the Westerbork sample of Paper II at the ≥ 1 mJy level.

The identification fraction of 41% $\pm$ 5% in the 0.2–5.0 mJy VLA sample is somewhat lower than the average percentage in the WSRT sample (53% $\pm$ 3% in the range 1–100 mJy), consistent with the gradual decreasing identification fraction on the 4 m plates at lower 1.4 GHz flux densities (Paper II). The fact that the overall identification fraction of radio sources with $S_{1.4} \approx 1$ mJy is as high as 50% suggests that the underlying population that causes the upturn in the 21 cm counts is already present among the identified sources. In the next section we will investigate which population(s), present among the millijansky identifications, could possibly cause the upturn in the source counts.

b) Photometry

i) *Object classification*

Below we analyze the four-band photometry following similar lines as in Paper III, where the photometry of the WSRT radio galaxies is discussed in conjunction with a few dozen spectroscopic redshifts. We will also compare the data on the sub-millijansky population to the millijansky sample of Paper III. Since the available spectroscopy of the sub-millijansky identifications is very limited (see notes to Table 2), we will concentrate on the photometry.

The basic diagram is the $J-F$ versus F color-magnitude diagram (Fig. 5). To illustrate the difference between the VLA and WSRT radio galaxy populations, we give in Figure 5*b* the $J-F$ versus F diagram for the WSRT sample (Fig. 3*a* of Paper III). In Paper III a distinction was made between red and blue radio galaxies. The brighter red radio galaxies were found to be exclusively giant ellipticals, whereas the brighter blue radio galaxies were found to be mostly ordinary spirals. For fainter radio galaxies, a similar empirical distinction could be made, although with less detailed morphological information and with less complete spectroscopic data; in general, the faint blue radio galaxies have an optical appearance that is unlike that of giant elliptical galaxies.

The redshift-magnitude diagram of Paper III showed that red galaxies are all luminous, following a Hubble relation with $M_F \approx -23.2 \pm 0.5$. In contrast, blue galaxies with $F < 16.5$ are spirals with $M_F \approx -21$. The blue galaxies with $F > 16.5$ are generally of more complex optical morphology, viz., double, interacting, or merging, or sometimes compact galaxies. Their *radio* powers, log $P_{1.4} \approx 23.5$, are much higher than those of ordinary spirals, while their *optical* luminosities are comparable to those of spiral galaxies. In Paper III, these blue radio galaxies are referred to as *B* galaxies; the red radio galaxies as *R* galaxies. In our Figure 5*a* we use the same distinction as in Paper III between *R* galaxies (*circles*) and *B* galaxies (*triangles*). This distinction is given by the full-drawn lines in Figure 5*a*, and for $F > 18$ the slope of the slanted line to first order accounts for the difference in *K*-correction between the giant elliptical and the *B* galaxy population at fainter magnitudes.

In Paper III an *a posteriori* supporting argument for the distinction of the radio galaxy population into *R* and *B* galaxies was found in the radio source morphology and their flux density. In Figures 5*a* and 5*b* interior-filled circles denote resolved radio sources (HPBW = 14″.7 for the VLA or HPBW [R.A.] = 12″.5 for the WSRT). In the VLA sample of Figure 5*a*, superposed crosses denote radio sources with $S_{1.4} > 1$ mJy, while in the WSRT sample of Figure 5*b*, crosses are drawn for $S_{1.4} > 9$ mJy. (Unless stated otherwise, the symbols of Fig. 5*a* apply to all other figures.) In the WSRT sample of Paper III

FIG. 5.—$J-F$ color vs. F magnitude for radio galaxies in the current VLA sample of Lynx.2 compared with the Leiden-Berkeley Deep Survey sample. (*a*) *The complete VLA radio galaxy sample in Lynx.2.* The classes "G" and "G?" are plotted as circles (red or *R* galaxies) and triangles (blue or *B* galaxies). The solid line separating these two classes is defined in Paper III. Squares are for objects of class "?." Sources resolved at 21 cm (HPBW = 12–15″) are marked by an interior filled circle. Sources stronger than $S_{1.4} = 1$ mJy have a superposed cross. Top solid curve is the predicted relation of Bruzual A. (1983) for a *nonevolving* giant elliptical with $M_V = -23.3$, $H_0 = 50$ km s^{-1} Mpc^{-1}, $q_0 = 0$, and age = 16 Gyr. Upper dashed curve is a mildly evolving spectrum with $\mu = 0.7$, the fractional galaxy mass that is processed into stars during the first gigayear after formation, and is otherwise the same. The lower dashed curve is for $H_0 = 100$ km s^{-1} Mpc^{-1}, $q_0 = 0$, age = 9 Gyr, $\mu = 0.7$, and $M_F = -21.8$. Estimated completeness limits are $F = 22.7$, $J = 23.7$ (*dotted lines*). (*b*) *The complete LBDS radio galaxy sample of Paper III.* The same symbols and lines as in (*a*) are used, except that sources stronger than $S_{1.4} = 9$ mJy now have a superposed cross. (*c*)–(*f*) *The combined radio galaxy samples* (Westerbork LBDS and VLA Lynx.2), divided in four flux density intervals. *All* WSRT radio galaxies are denoted by open circles, the VLA radio galaxies by interior tripods. The lines are the same as for (*a*).

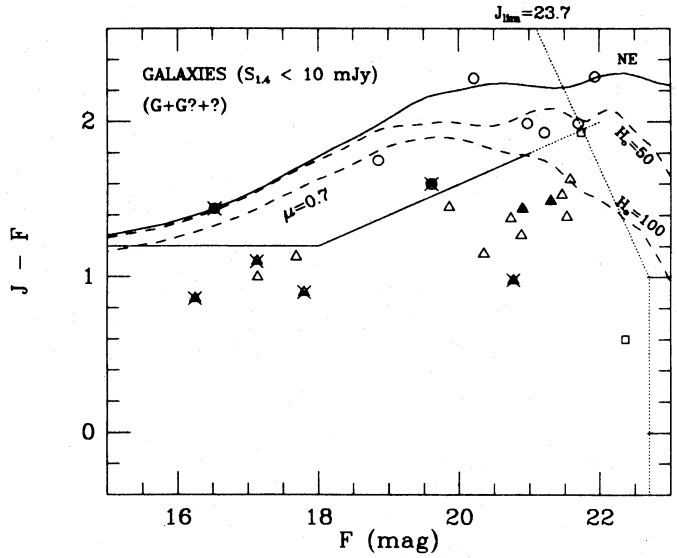

(a)

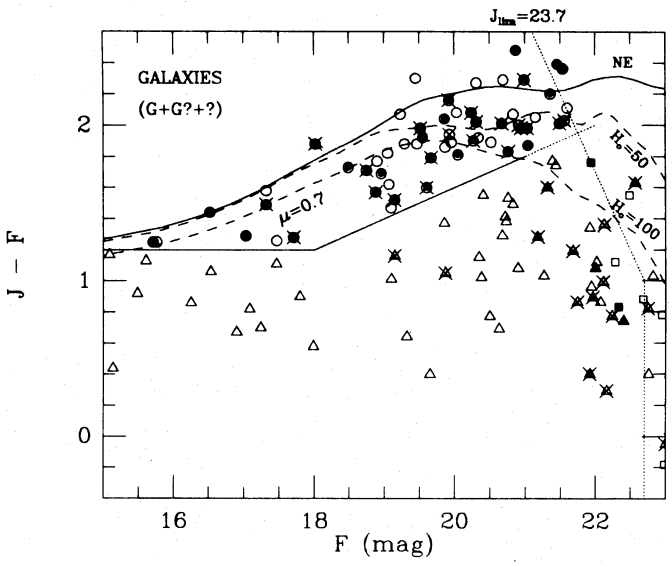

(b)

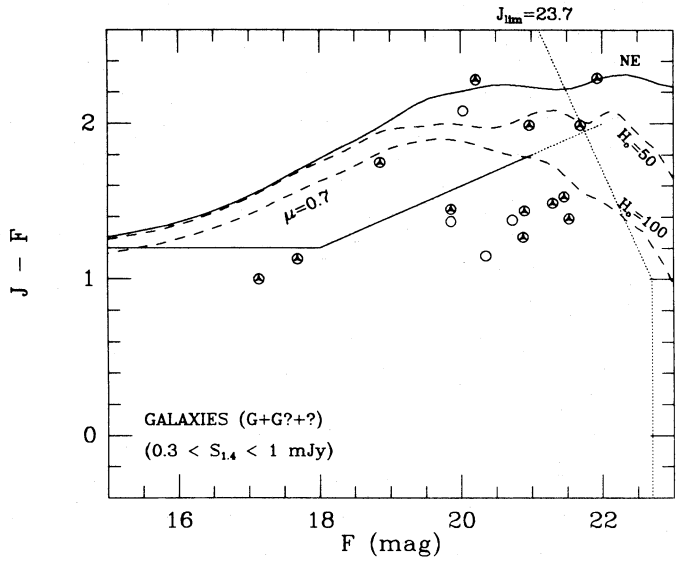

(c)

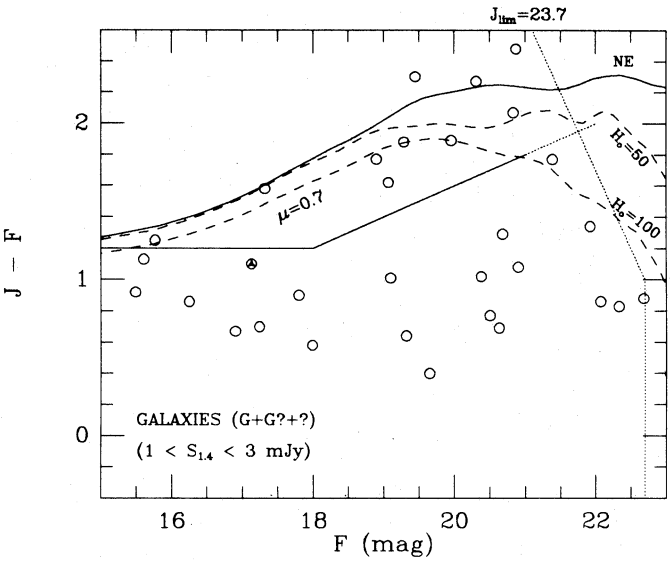

(d)

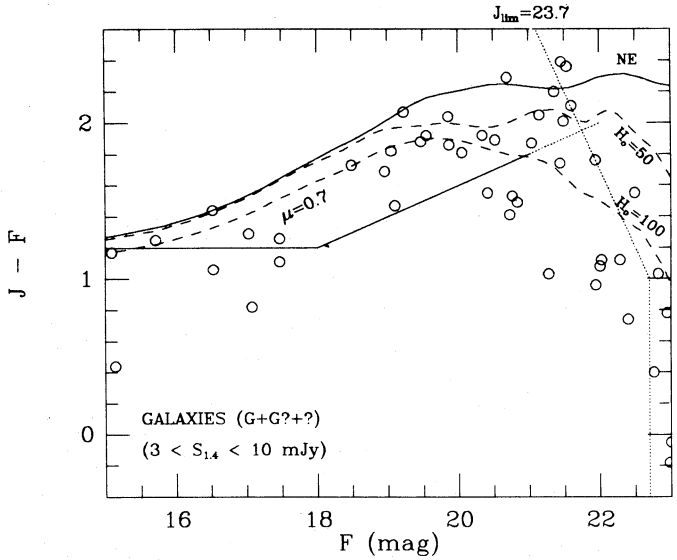

(e)

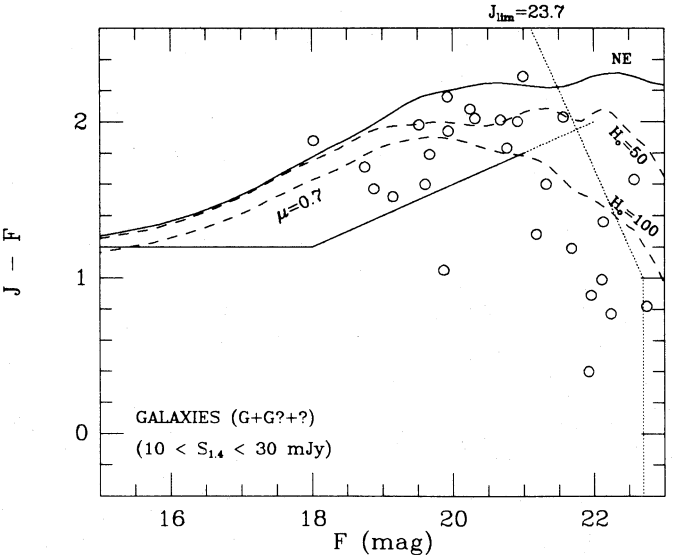

(f)

(our Fig. 5*b*) almost all radio sources that are resolved at the WSRT beam or that are stronger than $S_{1.4} \approx 9$ mJy turned out to be *R* galaxies, at least for $F < 21.5$. On the contrary, for $F < 21.5$ most *B* galaxies are unresolved radio sources and are fainter than 9 mJy. Note that there are some *B* galaxies associated with resolved radio sources in the VLA sample, while in Paper III most *B* galaxies, especially for $F \lesssim 21.5$ mag, are unresolved radio sources. This result could be due to some misclassified, unresolved sources in the sub-millijansky sample because of the broader wings in the VLA beam.

ii) *Color-Magnitude and Color-Color Diagrams*

Figure 5*a* shows that some *R* galaxies, presumably ellipticals, exist among the sub-millijansky radio sources. They have colors close to Bruzual's (1983) predictions for a nonevolving (*solid line*) or mildly evolving (Bruzual's parameter $\mu = 0.7$) elliptical (*dashed line*) spectral energy distribution that were computed for $H_0 = 50$ (or 100) km s^{-1} Mpc^{-1}, $q_0 = 0$, and galaxy age = 16 (or 9) Gyr. Also some bright spirals are seen for $F < 18$, $J - F < 1.2$, and about a dozen galaxies with blue colors similar to that of the *B* galaxy class of Paper III. The *relative* population density in the $J - F$ versus F diagram of the VLA sample, however, looks different from that of the brighter WSRT sample. The latter are mainly brighter than 1 mJy, with $S_{\rm median} \approx 5$ mJy; the VLA sources are mostly fainter than 1 mJy. In the WSRT sample, 54 *B* galaxies are seen and 66 *R* galaxies (including the 10 very red objects seen on the *F* and *N* plates only), while in the VLA sample, 16 *B* galaxies are found and only 9 *R* galaxies. Thus, *below 1 mJy a significantly larger fraction of faint B galaxies*, or fewer *R* galaxies, are seen.

It is interesting that the identification of radio source 12 is the only galaxy in the whole survey (including the WSRT sample) for which we observed a Seyfert 1 spectrum. This is qualitatively consistent with the models plotted in Figure 4*b*, which show that an unevolving space density of normal spiral and Seyfert galaxies is not sufficient to explain the upturn in the source counts at the millijansky level. Note, however, that some of the blue galaxies for which do not have spectra may turn out to be Seyfert galaxies and that any weak Hα component may not have been detected in the other spectra.

Figure 6*a* shows the $F - N$ versus F diagram with the same symbols as Figure 5*a*. Most *R* galaxies lie close to Bruzual's nonevolving prediction for giant elliptical galaxies, which is consistent with the result of Paper III in that they do not show evidence for drastic spectral evolution out to redshifts of ~ 0.6.

A color-color diagram can be used to get an impression of the sampled redshift range, at least in a statistical sense (Koo 1981). Figure 6*b* shows the $U - J$ versus $J - F$ color-color diagram for the intervals $21 < J < 22$ (*large symbols*) and $22 < J < 23$ (*small symbols*). The faint blue sub-millijansky galaxies are consistent with being at redshifts $\lesssim 0.5$, in accordance with the redshifts measured in Paper III for the *B* radio galaxies in the 1–10 mJy regime.

iii) *Color-Magnitude versus* 1.4 GHz *Flux Density*

The relative contribution of the *R* and *B* galaxies as a function of radio flux density is illustrated in Figures 5*c*–5*f*. These plots contain *both* the complete VLA *and* the complete WSRT sample (the brighter VLA sources already seen in the WSRT map of Lynx.2 are only plotted once). Let us consider the ratio of *B* to *R* galaxies ($r = n_B/n_R$), as counted in the complete samples above the plate limits. This ratio amounts to 11/5 ($r = 2.2 \pm 1.1$) for $0.3 < S_{1.4} < 1$ mJy, 21/10 ($r = 2.1 \pm 0.8$) for $1 < S_{1.4} < 3$ mJy, and decreases to 17/22 ($r = 0.78 \pm 0.25$) for $3 < S_{1.4} < 10$ mJy, and to 9/16 ($r = 0.56 \pm 0.23$) for $10 < S_{1.4} < 30$ mJy. Thus, while above 10 mJy the *B* galaxies are a minority at $\sim 35\%$ of all radio galaxies, they dominate the radio galaxy population at 70% below 3 mJy.

For the *R* and *B* galaxies, Figure 7 shows the relation between (monochromatic) radio and optical fluxes, F(mag) versus log $S_{1.4}$(mJy), with lines of constant radio-optical spectral index $\alpha_{\rm ro}$ (S_{21}/S_F in various powers of 10). Figure 7 shows that the *B* radio galaxy population has, on average, a somewhat lower $\alpha_{\rm ro}$ than the giant elliptical or *R* galaxies. The latter objects have $0.25 \lesssim \alpha_{\rm ro} \lesssim 0.50$, as shown in Paper III.

Figure 8*a* gives the $J - F$ color versus log $S_{1.4}$ for all WSRT radio galaxies and for those VLA radio galaxies that were not

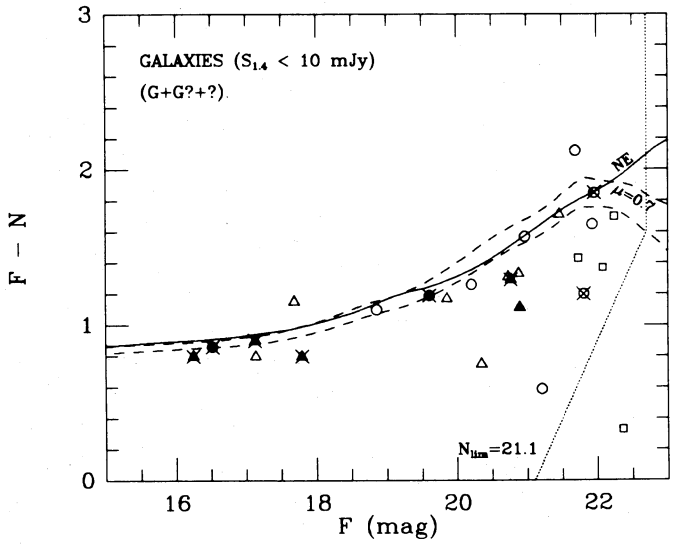

FIG. 6*a*

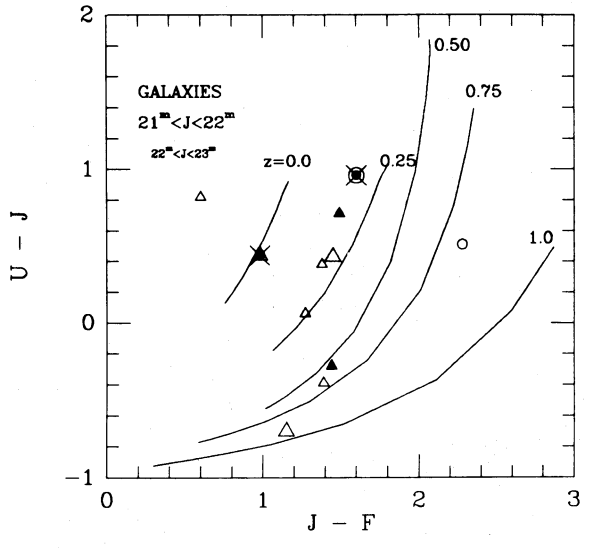

FIG. 6*b*

FIG. 6*a*.—$F - N$ color vs. F magnitude diagram for classes "G," "G?," and "?" in the radio-optical complete sample. The symbols and models are as in Fig. 5*a*.

FIG. 6*b*.—$U - J$ color vs. $J - F$ color-color diagram for all galaxies in the complete VLA sample with $21 \leq J \leq 22$ (*large symbols*) and $22 \leq J \leq 23$ (*small symbols*). The lines are loci of equal redshifts of the spectral evolution models of Bruzual (1983) with $0.01 < \mu < 0.9$ and for $H_0 = 50$ km s^{-1} Mpc^{-1}, $q_0 = 0$, and age = 16 Gyr at $z = 0$. Symbols are as in Fig. 5*a*.

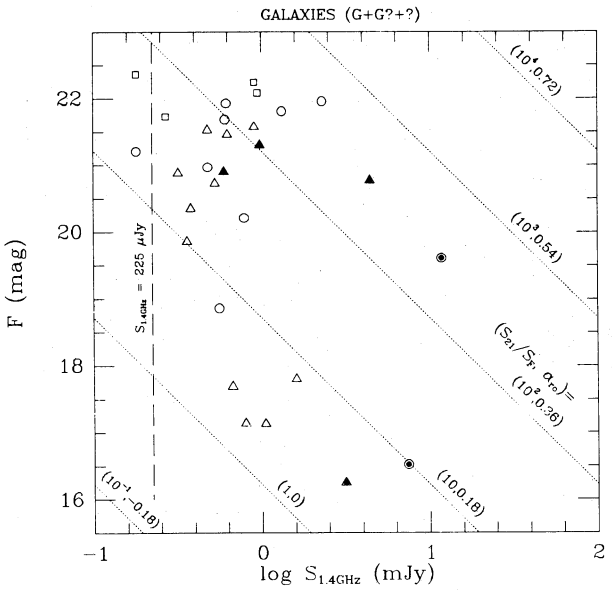

FIG. 7.—F magnitude vs. $S_{1.4}$ flux density for all radio galaxies in the complete VLA sample. For symbols, see the caption of Fig. 5*a*. Lines of constant radio-to-optical spectral index denote monochromatic radio-optical flux ratios $S(21\text{ cm})/S(6100\text{ Å}) = 10^{-1}$, 1, 10, 10^2, 10^3, and 10^4 with corresponding radio-optical spectral index $\alpha_{ro} = -0.18, 0, 0.18, 0.36, 0.54$, and 0.72.

already detected in the WSRT Lynx.2 map. In Figure 8*a* a morphological distinction is made for $F < 19$ between bright spiral or B galaxies (*triangles*) and bright (giant) elliptical galaxies (*circles*). Note that in a survey of 5.5 deg^2 bright spirals occur only for $S_{1.4} \lesssim 10$ mJy. It is stressed that objects have different weights as a function of $S_{1.4}$ because of differential primary beam effects. For instance, a detected WSRT source around 1 mJy represents in fact, about five sources within 5.5 deg^2, while a VLA source detected around 0.25 mJy represents ~ 50 sources in 5.5 deg^2 (a factor of 5 due to the limited visibility within the VLA primary beam and another factor of 10 since the total VLA area is $\sim 1/10$ of the total area covered by the LBDS). However, within a small flux density bin the *relative* number of sources should be representative. (For $S_{1.4} \gtrsim 5$ mJy all weights approach unity.) In Figure 8*b* the same diagram is shown, but the distinction between R (*circles*) and B (*triangles*) galaxies is now made for *all* galaxies as defined in Figures 5*a* and 5*b*. This distinction is *not* independent information in a diagram with $J-F$ as one of the axes, but it does give an impression how the relative contribution of the R and B galaxies varies *within* different flux density bins. The inclusion of the faintest radio galaxies ($F > 21.5$) in Figures 8*a* and 8*b* does not significantly broaden the distribution along the $J-F$ axis.

Figures 8*a* and 8*b* should be studied in conjunction with the source counts in Figure 4*b*, which has the same horizontal scale. As also noted from Figures 5*c*–5*f*, the fraction of B radio galaxies increases from about one-third at flux densities in excess of 10 mJy to about two-thirds around and below 3 mJy, where the upturn in the source counts occurs. In conclusion, at $S_{1.4} \lesssim 5$ mJy, where the change in the slope of the source counts becomes evident, the B radio galaxy population starts to dominate the radio source identifications.

We note that very few radio galaxies exist with $0.25 < S_{1.4} < 1$ mJy *and* $J-F \lesssim 1$, while many exist for $J-F \gtrsim 1$. This apparent lack of very blue sub-millijansky galaxies is even more pronounced if we recall that selection effects are in favor of B galaxies for $S_{1.4} < 1$ mJy. This is because the J plate limit (Figs. 5*a*, 5*b*) operated against faint R galaxies, while spurious identifications will be mainly faint blue field galaxies, occurring predominantly among the very faint radio sources with the largest position errors. An explanation could be the following. The closer ($z \approx 0.2$) and therefore bluer ($J-F < 1$) sub-millijansky radio galaxies do exist, but are not sampled (or just barely) because of the limited volume of the VLA survey. Their more distant ($z \approx 0.4$) and thus somewhat redder ($J-F \approx$ 1.2–1.5) counterparts show up in larger numbers, at least in part because of the larger volume sampled. With more redshifts we will investigate whether this is also due to possible cosmological evolution at radio wavelengths of the B galaxies, in the sense that they were more frequent or more powerful radio sources in the past.

Another possible explanation for the apparent lack of very blue sub-millijansky galaxies is that the colors of the faint B galaxies may be correlated with radio power in the sense that B galaxies of weaker radio power have relatively redder colors.

VI. DISCUSSION AND CONCLUSIONS

The available 1.4 GHz source count data yield the following picture. The normalized differential 21 cm source counts show strong convergence in the range 1000 → 10 mJy, attributed to the epoch-dependent radio luminosity function of giant elliptical galaxies and quasars, both of which evolve more strongly for the higher radio powers. Below 5 mJy a gradual flattening in slope occurs. The slope of the normalized differential counts $[(dN/dS)/225S^{-2.5}]$ changes from ~ 0.7 (or $\gamma \approx 1.8$, if $dN/dS \propto S^{-\gamma}$) in the range 100–5 mJy to ~ 0.4 ($\gamma \approx 2.1$) in the range 5–0.25 mJy. This upturn is not likely to be due to systematic errors, unless these occur in the *same* way in *different* surveys with *different* instruments at *different* signal-to-noise levels. It is not likely to be entirely due to field-to-field variations either, because otherwise the VLA and WSRT counts in Lynx should differ significantly from the ones in Condon and Mitchell's area at *all* flux levels.

The optical identification statistics and content at the sub-millijansky level are not drastically different from those at the millijansky level in the WSRT sample. The sub-millijansky radio source population seems to comprise a few galactic stars, some quasars, red radio galaxies, and a blue radio galaxy population. The latter are mainly spiral galaxies at brighter magnitudes, but at fainter magnitudes they are probably like the faint blue radio galaxies of Paper III (peculiar, interacting, sometimes merging, or compact galaxies). In Paper III these B galaxies were shown to have radio powers about a decade higher than those of normal spiral galaxies. In this context, we note that double galaxies (Hummel 1981) and mergers (Heckman 1983) both have statistically higher radio powers when compared to normal spiral galaxies.

A comparison of the photometry of the sub-millijansky VLA sample with the millijansky WSRT sample shows that the fraction of B radio galaxies changes from 35% at levels brighter than 10 mJy to $\sim 70\%$ below 3 mJy. Thus, where the change in the slope of the source counts occurs, the B galaxy population becomes increasingly dominant. It is plausible that the B galaxies cause the upturn in the 1.4 GHz counts below a few millijanskys. It should be remembered that the nature of the *unidentified* sub-millijansky radio sources is unknown as yet.

There is an apparent lack of very blue ($J-F < 1$) galaxies below 1 mJy, possibly because B galaxies below 1 mJy have

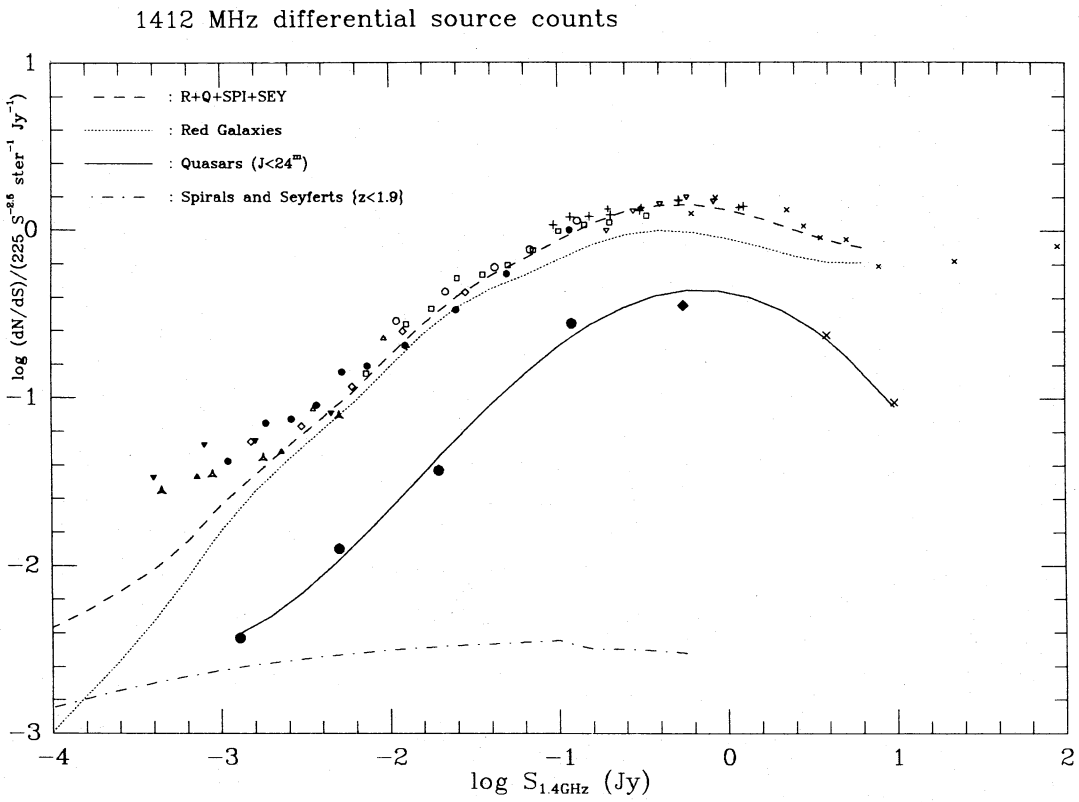

FIG. 4*b*.—Comparison of the 1.4 GHz counts with known populations. Data and symbols are the same as in Fig. 4*a* (see page 507), except that the few nonindependent and incomplete points are omitted. All error bars are omitted to prevent overcrowding. Shown are the predicted counts for the nonevolving Seyfert and spiral radio galaxies (*dot-dash*), giant elliptical radio galaxies (*dotted*), and radio quasars with $B < 24$ (*solid*) as well as their sum (*long dash*). Models are from Windhorst (1984).

FIG. 8*a*.—$J-F$ color vs. $S_{1.4}$ flux density for the *combined* complete WSRT (LBDS) and VLA (Lynx.2) samples of radio galaxies. A *morphological* distinction is given for the few objects with $F < 19$ by superposed symbols: open circles denote bright (giant) elliptical galaxies; open triangles, bright spiral or B galaxies. 8*b*.—$J-F$ color vs. $S_{1.4}$ flux density for the *combined* complete WSRT (LBDS) and VLA Lynx.2 samples of radio galaxies. Open circles denote R galaxies, open triangles denote B galaxies, according to the definition in Fig. 5*a*. (For $F < 19$, these correspond to bright giant elliptical and spiral galaxies, respectively; see Fig. 8*a*). Interior-filled circles denote resolved radio sources, which are mainly associated with R galaxies. For $S_{1.4} < 10$ mJy the B galaxies become apparently more dominant *per flux density bin*. For $S_{1.4} < 1$ mJy the B galaxies still exist, but are mainly redder than $J-F = 1.0$.

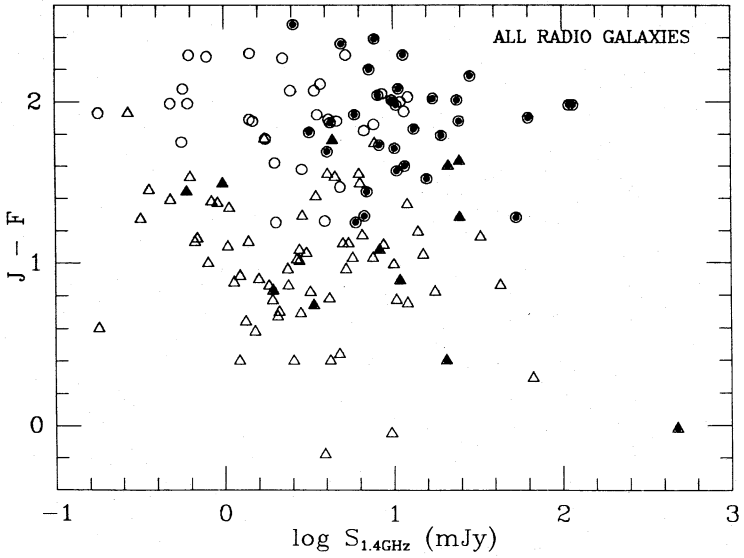

FIG. 8*a*

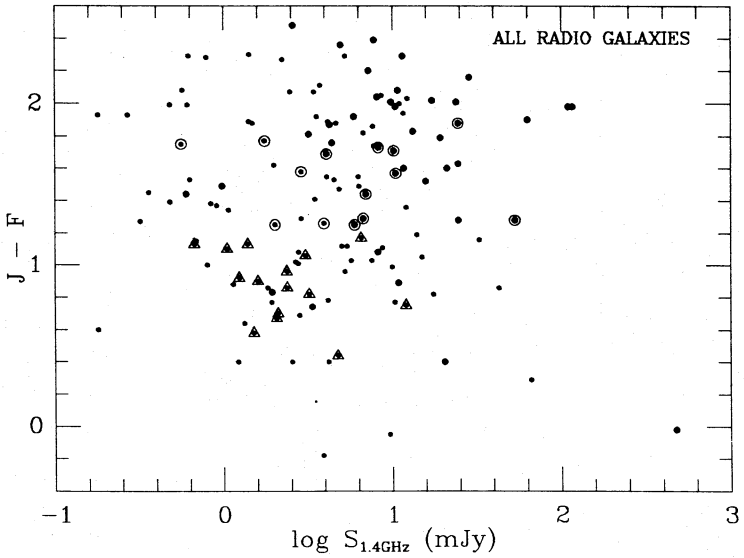

FIG. 8*b*

appreciable redshifts, where K-corrections result in redder $J-F$ colors. Combined with the resteepening of the counts, this result may indicate that the B galaxies have undergone population evolution similar to that of the giant elliptical galaxies and quasars, but at levels ~ 1000 times weaker in radio power, thus showing up at radio flux densities ~ 1000 times fainter. The flattening in the differential source counts below 5 mJy would then be analogous to the well-known initial steep rise in strong source counts just below 10 Jy (Ryle 1957; Bridle *et al.* 1972). This possibility must be investigated with more spectroscopy for the B galaxies.

In addition, a determination of the radio morphologies and radio spectra of a sample of our faint sources would be fruitful. To this end, VLA measurements at 21 cm with the A-configuration would give resolutions of $\sim 1''$ which would allow us to study whether the weak sources have the scale of a galactic disk, or are dominated by kiloparsec-scale components, such as those suggested by Heckman *et al.* (1983). Such a program is currently being undertaken with the VLA for the LBDS radio galaxies (Oort, Katgert, and Windhorst, in preparation).

We gratefully acknowledge the National Radio Astronomy Observatory and Kitt Peak National Observatory for the generous allocation of telescope time. The National Radio Astronomy Observatory is operated by Associated Universities, Inc., under contract with the National Science Foundation. Kitt Peak National Observatory is operated by the Association of Universities for Research in Astronomy, Inc., under contract with the National Science Foundation.

This work was partially supported by NSF grants 79 90994 and 81 21653 of the United States. R. A. W. acknowledges the Netherlands Organization for the Advancement of Pure Research (ZWO) for ASTRON/ZWO grant 19-23-009 and a travel grant.

We thank Klaas Lugtenborg and Klaas Weerstra for adapting the Charlottesville IBM package to our special needs and Bill Schoening for help with the photographic process. Donald Hamilton provided assistance with the photometry software and Marc Oort with the model calculations. Allan Sandage kindly made available his photoelectric sequence in the Lynx field. R. A. W. wishes to thank Harry van der Laan and Peter Katgert for stimulating discussions and their continuous support of the project.

The manuscript was typed patiently by Maria Anderson and Wanda van Grieken, the photographs were prepared carefully by Richard Dreiser and Wim Brokaar, and the drawings were made efficiently by Sjaak Ober and VAX 11/750.

REFERENCES

Auriemma, C., Perola, G. C., Ekers, R. D., Fanti, R., Lari, C., Jaffe, W. J., and Ulrich, M.-H. 1977, *Astr. Ap.*, **57**, 41.
Baars, J. W. M., Genzel, R., Pauliny-Toth, I. I. K., and Witzel, A. 1977, *Astr. Ap.*, **61**, 99.
Bridle, A. H., Davis, M. M., Fomalont, E. B., and Lequeux, J. 1972, *A.J.*, **77**, 405.
Bruzual, A. G. 1983, *Ap. J.*, **273**, 105.
Condon, J. J., and Mitchell, K. J. 1982, *A.J.*, **87**, 1429.
de Ruiter, H. R., Willis, A. G., and Arp, H. C. 1977, *Astr. Ap. Suppl.*, **28**, 211.
Ekers, R. D., and Miley, G. K. 1977, in *IAU Symposium 74, Radio Astronomy and Cosmology*, ed. D. L. Jauncey (Dordrecht: Reidel), p. 109.
Heckman, T. M. 1983, *Ap. J.*, **268**, 628.
Heckman, T. M., van Breugel, W., Miley, G. K., and Butcher, H. R. 1983, *A.J.*, **88**, 8.
Hummel, E. 1980, Ph.D. thesis, University of Groningen.
———. 1981, *Astr. Ap.*, **96**, 111.
Katgert, P., Katgert-Merkelijn, J. K., Le Poole, R. S., and van der Laan, H. 1973, *Astr. Ap.*, **23**, 171.
Katgert-Merkelijn, J., Lari, C., and Padrielli, L. 1980, *Astr. Ap. Suppl.*, **40**, 91.
Koo, D. C. 1981, Ph.D. thesis, University of California, Berkeley.
Kron, R. G. 1980, *Ap. J. Suppl.*, **43**, 305.
Kron, R. G., Koo, D. C., and Windhorst, R. A. 1984, *Astr. Ap.*, in press (Paper III).
Meurs, E. J. A. 1982, Ph.D. thesis, University of Leiden.
Murdoch, H. S., Crawford, D. F., and Jauncey, D. L. 1973, *Ap. J.*, **183**, 1.
Napier, P. J., and Rots, A. H. 1982, VLA Test Memorandum, No. 134.
Oort, M. J. A., and Windhorst, R. A. 1984, *Astr. Ap.*, in press.
Oosterbaan, C. E. 1978, *Astr. Ap.*, **69**, 235.
Ryle, M. 1957, in *IAU Symposium 4, Radio Astronomy*, ed. H. C. van der Hulst (Cambridge: Cambridge University Press), p. 221.
Thompson, A. R., Clark, B. G., Wade, C. M., and Napier, P. J. 1980, *Ap. J. Suppl.*, **44**, 151.
van der Laan, H., Katgert, P., Windhorst, R. A., and Oort, M. J. A. 1983, in *IAU Symposium 104, The Early Evolution of the Universe and its Present Structure*, ed. G. O. Abell and G. Chincarini (Dordrecht: Reidel), p. 73.
van der Laan, H., and Windhorst, R. A. 1982, in *Astrophysical Cosmology: Proceedings of the Vatican Study Week on Cosmology and Fundamental Physics*, ed. H. A. Brück, G. V. Coyne, and M. S. Longair (Vaticano: Pontificiae Academiae Scientarum), p. 349.
Willis, A. G., Oosterbaan, C. E., Le Poole, R. S., de Ruiter, H. R., Strom, R. G., Valentijn, E. A., Katgert, P., and Katgert-Merkelijn, J. K. 1977, in *IAU Symposium 74, Radio Astronomy and Cosmology*, ed. D. L. Jauncey (Dordrecht: Reidel), p. 39.
Windhorst, R. A. 1984, Ph.D. thesis, University of Leiden.
Windhorst, R. A., Kron, R. G., and Koo, D. C. 1984, *Astr. Ap. Suppl.*, **58**, 39 (Paper II).
Windhorst, R. A., van Heerde, G. M., and Katgert, P. 1984, *Astr. Ap. Suppl.*, **58**, 1 (Paper I).

RICHARD G. KRON: Yerkes Observatory, University of Chicago, Williams Bay, WI 53191

DAVID C. KOO and GEORGE K. MILEY: Space Telescope Science Institute, Homewood Campus, John Hopkins University, Baltimore, MD 21218

FRAZER N. OWEN: National Radio Astronomy Observatory, P.O. Box O, Socorro, NM 87801

ROGIER A. WINDHORST: Mount Wilson and Las Campanas Observatories, 813 Santa Barbara Street, Pasadena, CA 91101

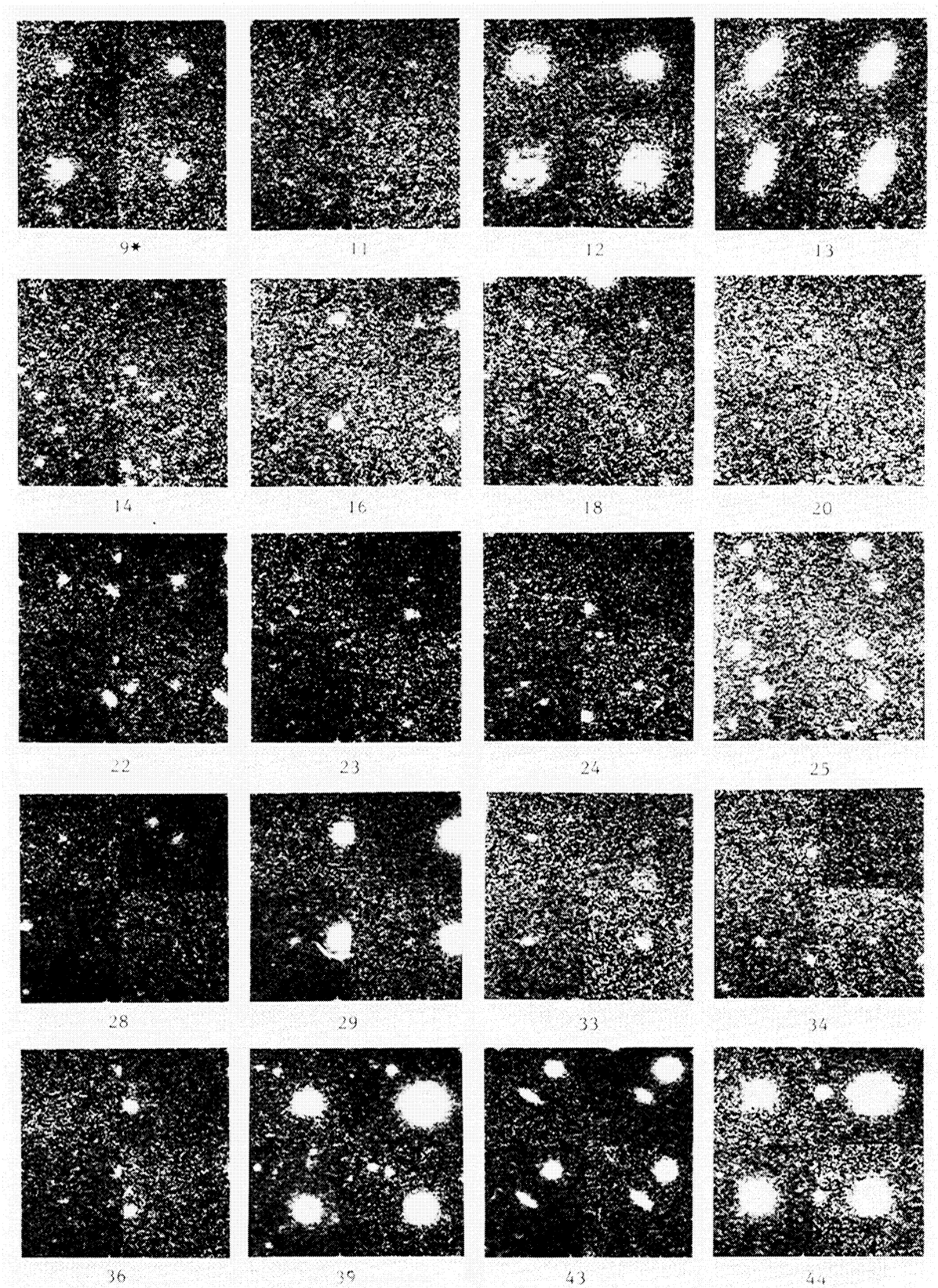

FIG. 3.—Multiband images of the identified radio sources, in order of sequence number in the VLA source list. For each source the *U* image is in the lower left, *J* in lower right, *F* in upper left, and *N* in the upper right quadrant. The area around each image is 30″ on a side, except that the *U* and *F* images are cut off slightly at the left side. North is up, east is to the left. For each source the identification is centered. Defects exist on the *U* frame of No. 29 and on the *N* frame of No. 75. A satellite trail crosses the *N* frame of No. 107A. The limited dynamic range of these pictures must be kept in mind when evaluating galaxy morphology (for this purpose, the finding charts in Paper II are superior).

WINDHORST *et al.* (*see* page 503)

PLATE 6

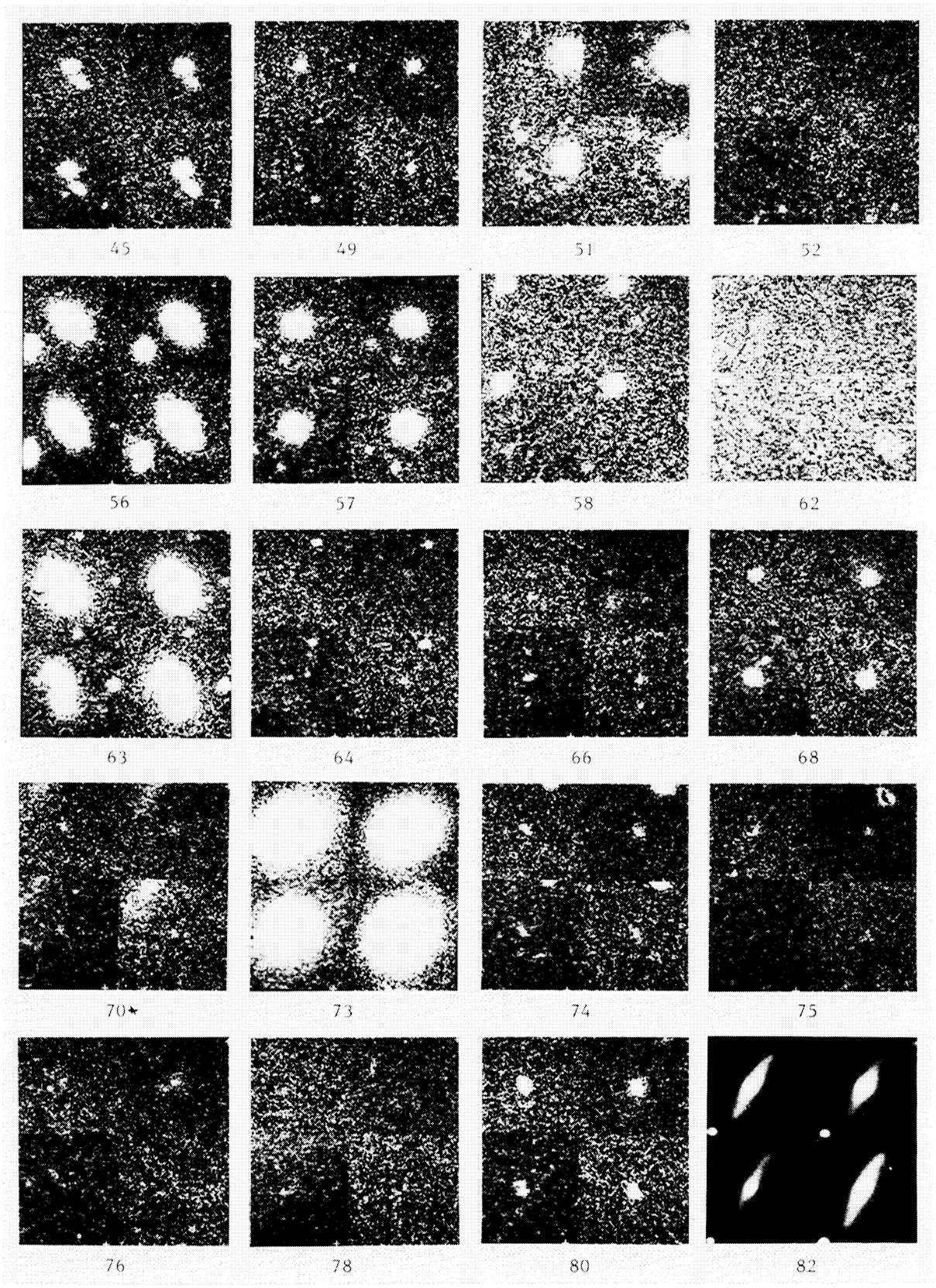

FIG. 3.—*Continued*

WINDHORST *et al.* (*see* page 503)

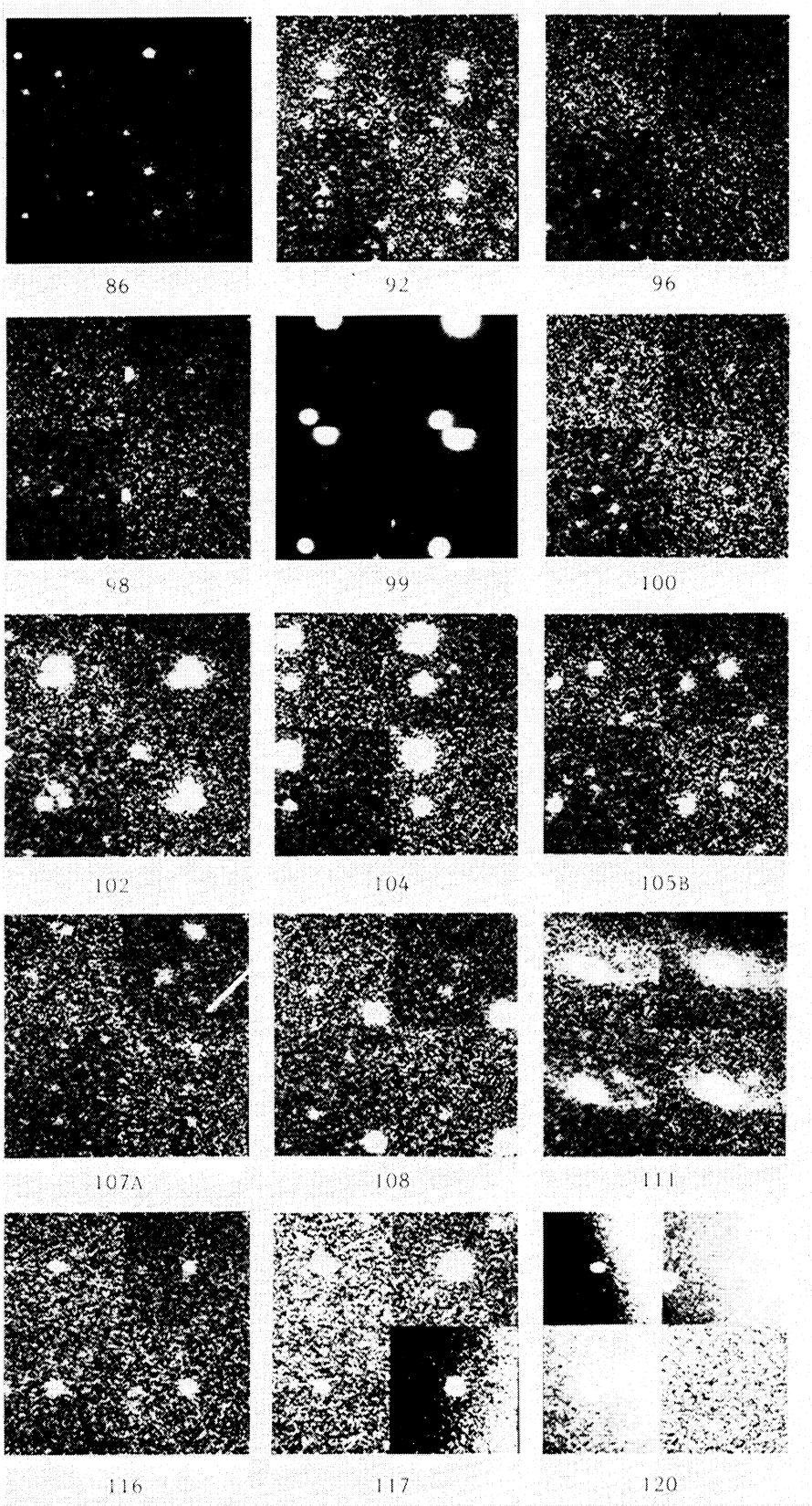

FIG. 3.—*Continued*